Retinal and choroidal capillary imaging by optical coherence tomography

Retinal and choroidal capillary imaging by optical coherence tomography

Kazuhiro Kurokawa
Doctoral Program in Applied Physics

Submitted to the Graduate School of
Pure and Applied Sciences
in Partial Fulfillment of the Requirements
for the Degree of Doctor of Philosophy in
Engineering

at the
University of Tsukuba

Acknowledgment

Six years has passed since I joined Computational Optics Group (COG) as an undergraduate student in the University of Tsukuba. I finally understood that I'm a really fortunate to work with a nice group of people. I would like to thank all of the COG members and ex-members. In addition, I realized that I was not able to continue my research without a lot of help from excellent researchers anywhere in the world. I would like to thank all the people for having a discussion, question, suggestion, and encouragement.

I would like to express my gratitude to Dr. Yoshiaki Yasuno, who is an outstanding engineer, researcher, and leader of COG. Without his kindness, instruction, and support, I was not able to continue my research. I was lucky to have such a grateful mentor. I would like to gratefully thank Dr. Shuichi Makita, who gives me a lot of helpful and practical advices. Without his instruction, I was not able to understand my research more concretely.

I would like to thank all the committee members, Prof. Masahide Itoh, Prof. Tetsuro Oshika, Prof. Norio Watanabe, Prof. Hideaki Kanou, and Prof. Takeshige Omatsu. I would like to thank Prof. Masahide Itoh, who is an official adviser, for guiding me to focus on the research. In addition, I would like to thank Prof. Masahiro Miura for teaching ophthalmic medicine, especially about retinal imaging. I would like to thank Prof. Barry Cense and his laboratory members in Utsunomiya University for having fruitful discussions. I would like to thank Prof. Shuliang Jiao and Xiangyang Zhang in the University of South California to give an opportunity for my internship. It was my precious experience. I would like to thank Dr. Laurent Vabre in Imagine Eyes for the technical support and encouragement.

I would like to thank the COG members and ex-members: Young-joo Hong, Lian Duan, Kazuhiro Sasaki, Yiheng Lim, Arata Miyazawa, Franck Jailon, and Masahiro Yamanari. I also thank temporal members: Myeong Jin Ju and Daiki Tamada. All COG members are kind, quite patient and hard workers. I have learned enormous things from them. They are colleagues, however, at the same time, they are extraordinary mentors. Especially, Kazuhiro Sasaki had an important part in this research. His effort was invaluable and helpful.

I would like to thank anonymous reviewers and excellent researchers somewhere in the world for having a discussion, question, suggestion, and encouragement. They pointed out very accurately and suggested me a lot of valuable experiments.

Finally, I would like to give a special thanks to my family and friends.

Abstract of dissertation

Optical coherence tomography (OCT) provides the axial profile of backscattered light from the sample and enables non-invasive, three-dimensional retinal imaging. Therefore, OCT has shown its powerful utility especially in the field of ophthalmology. On the other hand, however, there is still a lot of room to improve the imaging ability of opthalmic OCT.

Recent development of ophthalmic OCT has shown the enhanced image contrast at the deep region of the eyes using a 1-μm probe. In addition, several types of high-speed swept-laser source become available at 1-μm wavelength band. At the same time, adaptive-optics (AO) has been used to further enhance the lateral resolution of ophthalmic OCT. Therefore, we expected AO-OCT using a 1-μm probe (1-μm AO-OCT) is capable of high-resolution and high-speed posterior-eye imaging with high-penetration property. Furthermore, several OCT-based angiographic methods have shown its powerful utility in the detection of micro-vasculature. By combining these techniques, we speculated that the posterior-eye imaging ability can be further enhanced.

The aim of this dissertation is to demonstrate the retinal and choroidal capillary imaging by OCT. For that purpose, the imaging ability of ophthalmic OCT is enhanced by developing 1-μm AO-OCT and implementing several multiple-volume OCT-based angiographic algorithms.

First, we developed 1-μm AO-OCT from the optical design. The system performance was evaluated numerically and experimentally. Furthermore, in order to extend the focal range, we created the spherical aberration on the pupil plane in addition to the cancellation of the ocular monochromatic aberration. The effect of spherical aberration was again evaluated numerically and experimentally. Finally, *in vivo* photoreceptor imaging performance was investigated. In total, four eyes of 4 subjects were examined. The image qualities were qualitatively and quantitatively assessed. The results showed clear photoreceptor cells at 4-5 degree Nasal with AO. The RMS wavefront errors were reduced to be less than 0.1 μm. We qualitatively found that the negative-SA of 0.4 μm in RMS provides slight better image quality than non-SA and positive-SA of 0.4 μm in RMS.

Second, several multiple-volume OCT-based angiographic algorithms were used to further enhance the vasculature image quality. We calculated averaged intensity, amplitude decorrelation, and averaged power of Doppler shift. Six eyes of 6 subjects were examined by the of a phase-stabilized swept-source OCT (SS-OCT). The results showed high-contrast three-dimensional retinal and choroidal micro-vasculature images for all eyes. In the retina, the slight change of vasculature image quality was found between the angiographic algorithms. However, in the case of the choroid, the choroidal capillary networks

in the Sattler's layer were more clearly contrasted by the averaged Doppler algorithm than the others.

Finally, in order to observe more details, high-resolution retinal and choroidal capillary imaging has been demonstrated. Four eyes of 4 subjects were examined by 1-μm AO-OCT. The results showed the depth-resolved capillary network clearly. In the retina, the slight change of capillary image quality was found between the angiographic algorithms. However, the choriocapillaris were rarely visible in the averaged intensity image, though the other angiographic algorithms showed the capillary network clearly.

In conclusion, we successfully enhances the capillary imaging performance of ophthalmic OCT by developing 1-μm AO-OCT and using several multiple-volume OCT angiographic algorithms. It was found that the combination of Doppler techniques and AO-OCT is especially useful for the detection of choriocapillaris. In addition, the combination of SS-OCT and 1-μm AO-OCT is capable of a more comprehensive vascular and structural imaging for the medical diagnosis.

Contents

List of Figures

List of Tables

Chapter 1

Introduction

Optical coherence tomography (OCT) provides the axial profile of backscattered light from the sample and enables depth-resolved retinal imaging [1]. Further, frequency-domain OCT (FD-OCT) has a higher sensitivity and acquisition speed than time-domain OCT (TD-OCT) [2–5] and enables three-dimensional retinal imaging. Therefore, FD-OCT has shown its powerful utility especially in the field of ophthalmology [6].

Posterior-eye imaging is an important application of ophthalmic OCT, since several severe eye diseases, such as glaucoma, age-related macular generation, degenerative myopia, and diabetic retinopathy, are known to be related with the structural deformation and malfunction of the posterior-eye [7–9]. Thus, ophthalmic OCT has been widely used for the detection of such structural deformation. On the other hand, however, there is still a lot of room to improve the imaging ability of opthalmic OCT. In order to further enhance the imaging ability, there are several approaches.

For instance, adaptive-optics (AO) technology is used to enhance the lateral resolution of ophthalmic OCT. Since AO improves the lateral resolution by correcting the ocular monochromatic aberration [10], AO-OCT allows *in vivo* microscopic investigation of the retina and choroid with extremely high lateral and axial resolution [11–14].

Another example is OCT-based angiography, which is used to enhance the image contrast of retinal and choroidal vasculature [15–29]. They reveals the tree-dimensional microvascular network, and have shown its utility to detect the vascular abnormalities.

One more example is a high-penetration OCT (HP-OCT), which is used to enhance the image contrast at the deep region of the eye using a center wavelength of a 1-μm probe [15, 30–33]. This is mainly because the 1-μm probe have less absorption property of retinal pigment epithelium (RPE) than 840-nm probe [15, 31, 34]. Hence, HP-OCT is more suitable for the detection of the choroidal feature.

The aim of this dissertation is to demonstrate the retinal and choroidal capillary imaging by OCT. For that purpose, the imaging ability of ophthalmic OCT is enhanced by developing AO-OCT using a 1-μm probe (1-μm AO-OCT) and implementing several multiple-volume OCT-based angiographic algorithms.

1.1 Frequency-domain OCT

In this section, the principle of frequency-domain OCT (FD-OCT) is briefly described [35].

OCT is based on a low coherence interferometry [2, 36]. Hence, a temporally low-coherence light source is used. Since the coherence length is short, the limited number of photons, which is within a "coherence gate", make the interference. Thus, the depth resolution of the OCT is limited by the coherence length of light source. If the light source have a Gaussian shape spectrum, the round trip coherence length Δl is defined as

$$\Delta l = \frac{2ln(2)}{\pi}\frac{\lambda_c}{\Delta\lambda}, \tag{1.1}$$

where λ_c and $\Delta\lambda$ are the center wavelength and the spectral bandwidth of the light source, respectively. Typically, depth resolution of ophthalmic OCT is a few or a dozen micrometer.

In order to obtain the interference, the conventional types of interferometers can be used. Here, a Michelson interferometer is assumed for simplicity. First, the light from the source is delivered to the interferometer. Its wave function is described in complex form as, $E_{LS}(k, w) = s(k, w)\exp(i(wt - kz))$, where $s(k, w)$ is the amplitude function of the source as a function of wavenumber k and angular frequency w. Then, the light is split into the sample and reference arm. Here, we assumed the ideal splitting ratio of 50-50, and hence the input light for each arm is described as $\frac{E_{LS}}{\sqrt{2}}$.

In the sample arm, the input light illuminates the sample, and the backscattered light from the sample is collected. The wave function of the backscattered light can be described as $E_s = \frac{E_{LS}}{\sqrt{2}}\int a(z)\exp(i(wt - kz_s))dz$, where $a(z)$ is the back scattered amplitude coefficients of the sample. z_S is the optical path length of the sample arm. z is calculated by subtracting the optical path length of the reference arm from that of the sample arm.

In the reference arm, the light reflected from the mirror is collected. The wave function of the reflected light can be described as $E_s = \frac{E_{LS}}{\sqrt{2}}r_R\exp(i(wt - kz_R))$, where r_R is the amplitude reflectivity of the mirror, and z_R is the optical path length of the reference arm. Thus, $z = z_S - z_R$.

After collecting the lights from the sample and reference arm, they are recombined and interfered. Then, the detected spectral interferogram with a fixed time interval T is now described as

$$I(k) = S(k)|\frac{1}{\sqrt{2}}r_R\exp(-ikz_R) + \frac{1}{\sqrt{2}}\int a(z)\exp(-ik(z_R + z))dz|^2, \tag{1.2}$$

where $S(k)$ is the power spectrum of light source.

Since FD-OCT detect the spectral interferogram by encoding them in spatial or time domain, the inverse Fourier transform (IFT) of the detected spectral interferogram $I(k)$,

gives the axial profile of backscattering coefficients $a(z)$. When $z_R = 0$, the IFT of $I(k)$ is

$$\begin{aligned}\mathcal{F}^{-1}[I(k)](z) = \frac{1}{2}\rho V(z/c) \otimes \Big(& |r_R|^2 \delta(z) \\ & + A.C.[a(z)] \\ & + r_R^* a(z) + r_R a^*(-z) \Big),\end{aligned} \tag{1.3}$$

where ρ is the detector efficiency, $V(z/c)$ is the temporal coherence function of the light source, $A.C.[]$ is the auto-correlation operator. Here, the convolutions of temporal coherence function and DC (1st term), auto-correlation (2nd term) and cross-correlation terms (3rd and 4th terms) are obtained. The convolution of temporal coherence function and cross-correlation terms represent the complex OCT signals of backscattering light, more exactly speaking, the coherence sum of backscattering light from the scatterers in a coherence volume. Hence, the axial profile of backscattering coefficient of the sample ($z > 0$) can be obtained by taking the square of the complex OCT signal, which is described as $|\rho V(z/c) \otimes r_R^* a(z)|^2$.

1.2 OCT-based angiography

In this section, a brief summary of OCT-based angiographic methods is described.

The OCT-based angiographic methods are categorized as scattering OCT, speckle variance OCT, Doppler OCT, and auto-correlation. The methods are summarized in Table 1.1.

Scattering OCT represents the backscattering intensity of the samples as a function of the depth. Here, the intensity is described as $I(z) = |\Gamma(z)\Gamma^*(z)|$, where $\Gamma(z)$ is the complex OCT signal: $\Gamma(z) = \rho V(z/c) \otimes r_R^* a(z)$. Since the red blood cells is a hyper-scatterer, the micro-vasculature is appeared with hyper-scattering [16]. On the other hands, the large blood vessels are appeared with hypo-scattering, because the large blood vessels have a strong absorption [15, 17].

Speckle variance OCT represents the temporal changes of the backscattering coefficients of the sample [37, 38], so called "speckle variance". For instance, the speckle intensity variance can be described as

$$\sigma_I^2(z) = \sum_{i=1}^{N} \frac{(I_i(z) - \overline{I(z)})^2}{N}, \tag{1.4}$$

where $\overline{I(z)}$ is the averaged intensity. As a similar to the time-varying speckle analysis [39, 40], the velocity of the moving scatterers can be estimated [37, 38, 41].

Doppler OCT or optical Doppler tomography is a functional extension of OCT [42], and is utilized in retinal blood flow measurement [43–45]. In general, Doppler frequency shift of a moving scatter is described as $\Delta f_{Doppler} = 2v_{axial}/\lambda_c$, where v_{axial} is the axial velocity of the moving scatters parallel to the direction of the incident light. In order to obtain the Doppler frequency shift using OCT, several complex OCT signals are obtained

	Abbreviation	Symbol	References
Scattering OCT	Intensity	$I(z)$	[15–17]
Speckle variance OCT	Intensity variance Amplitude variance $\vdots$	$\sigma_I^2(z)$ $\sigma_{\sqrt{I}}^2(z)$ $\vdots$	[18, 19]
Doppler OCT	Fast Doppler mode Slow Doppler mode Dual-beam-scan Phase-shift variance	$\Delta\phi(z, \Delta t_{A-A})$ $\Delta\phi(z, \Delta t_{B-B})$ $\Delta\phi(z, \Delta t_{A-(A+n)})$ $\sigma_{\Delta\phi}^2(z)$	[42–45] [20–23, 46] [24, 25] [26, 27]
Auto-correlation	Doppler variance Amplitude decorrelation	$1 - \rho(z)$ $1 - \rho_{Amp}(z)$	[47, 48] [28, 29]

Table 1.1: Summary of OCT-based angiographic methods.

at the same region of interest. Then, phase-differences between complex OCT signals are calculated. Since the complex OCT signals are recorded separately at fixed intervals Δt, the axial velocity of moving scatters for each coherent volume is now described as

$$v_{axial,i} = \frac{\lambda_c}{4n\pi T}\Delta\phi_i, \tag{1.5}$$

where $\Delta\phi_i$ is given by $\Delta\phi_i(z, \Delta t) = \mathrm{Arg}\left[\Gamma_i(z,t)\Gamma_{i+1}^*(z, t+\Delta t)\right]$. Doppler flow sensitivity is mainly limited by the time interval Δt, Doppler angle, and phase noise. Here, the time intervals can be altered by modifying the scanning protocols [20–23, 46] or implementing dual-beam scan techniques [24, 25].

Auto-correlation method represents the temporal changes of the complex OCT signals. In general, auto-correlation coefficient of complex OCT signal is described as

$$\rho = \frac{\mathbf{E}[\Gamma_i(z,t)\Gamma_{i+1}^*(z, t+\Delta t)]}{\mathbf{E}[\Gamma(z,t)\Gamma^*(z,t)]}, \tag{1.6}$$

where $\mathbf{E}[x]$ denotes the expected value of x. As described by Zhao *et al.* and Wang *et al.* [47, 48], the sample motion during the fixed time interval Δt attenuates the auto-correlation coefficient, and hence the moving scatterers can be contrasted by $1 - \rho$. On the other hand, amplitude decorrelation is a modified version of the above mentioned method [28, 29]. The auto-correlation of amplitude of complex OCT signal was used to contrast the moving scatterers, which is described as $1 - \rho_{Amp}$.

1.3 Adaptive-optics

In this section, the basic principle of adaptive-optics (AO) is described [49]. Typically, AO technology is utilized to correct temporally and spatially aberrated wavefronts. In other word, AO dynamically improves the spatial coherence between sub-apertures on the pupil [50, 51].

In general, the AO system is consisted of a wavefront aberration measurement and correction parts. As an example, a Shack-Hartmann wavefront sensor (SHWS) is typically used for the wavefront aberration measurement, which is consisted of a lens-let array and CCD camera [52]. The wavefront aberration $W(x, y)$ is reconstructed by the spatially resolved slopes of the wavefront: $s_{x_j} = \frac{\partial W_j}{\partial x}$, $s_{y_j} = \frac{\partial W_j}{\partial y}$, where j is the index of sub-aperture. The slopes were estimated by calculating the centroids of the intensity profile for each sub-aperture. Then, the measured slope vector is described as

$$\mathbf{s} = [s_{x_1}, ...s_{x_j}, ...s_{x_N}, s_{y_1}, ...s_{y_j}, ...s_{y_N}]^T, \tag{1.7}$$

Since the slopes are measured by the intensity based method, the SHWS is achromatic and is available for the temporally incoherent light source.

Zernike standard coefficients $\mathbf{c}$ are given by the measured slope vector via a singular value decomposition (SVD). After the pupil center (x_0, y_0) and radius r are determined, the derivatives of Zernike standard polynomials are described as

$$\mathbf{s}_{x_n} = \frac{\partial}{\partial x} \sum_{n=0}^{N_{coef}} \sum_{m=-n}^{n} c_n^m Z_n^m (x, y) \tag{1.8}$$

$$\mathbf{s}_{y_n} = \frac{\partial}{\partial y} \sum_{n=0}^{N_{coef}} \sum_{m=-n}^{n} c_n^m Z_n^m (x, y) \tag{1.9}$$

where $Z_n^m(x, y)$ represents the Zernike standard polynomial after the change of coordinates and N_{coef} is the number of coefficients. Hence, the Zernike reconstruction matrix $\mathbf{Z}$ is given by $\mathbf{Z} = [\mathbf{s}_0, ..., \mathbf{s}_n, ..., \mathbf{s}_{N_{coef}}]$. Therefore,

$$\begin{aligned} \mathbf{s} &= \mathbf{Z}\mathbf{c} \\ \mathbf{c} &= \mathbf{Z}^+\mathbf{s} \end{aligned} \tag{1.10}$$

where $\mathbf{Z}^+$ is the Moore-Penrose pseudoinverse matrix of the derivatives of the Zernike standard polynomials. Here, the maximum number of Zernike coefficients N_{coef} is determined by the number of sub-apertures used for the wavefront reconstruction N [52], since the reliable Zernike order depends on how the slopes are densely sampled in the pupil. The maximum number of Zernike coefficients is approximately equal to the number of sub-apertures $N_{coef} \approx N$. In general, the Zernike order J is calculated by $N_{coef} = \frac{(J_+1)(J+2)}{2}$. Hence, the maximum Zernike order is calculated as $N \approx \frac{(J_{max}+1)(J_{max}+2)}{2}$.

As a part of the wavefront aberration correction, a membrane deformable mirror (DM) has been widely used, which is consisted of a membrane mirror and several actuators. The

command voltages are applied via a command vector $\mathbf{v}_m$, where m is the index of actuators.

In order to cancel the wavefront aberrations measured by the SHWS, the command vectors $\mathbf{v}$ are calculated by the Moore-Pensrose pseudo-inverse matrix of the influence matrix $\mathbf{A}^+$. The dimension of $\mathbf{A}$ is defined by the number of sub-apertures N and the number of actuators M. Thus, the command vector is given by $\mathbf{v} = \mathbf{A}^+\mathbf{s}$.

In practice, an integral controller is typically implemented to have a feedback loop [53], which is given by

$$\mathbf{v}_{t+T} = \mathbf{v}_t - \alpha\mathbf{A}^+\mathbf{s}_T, \tag{1.11}$$

where t is time, T is a period of a single cycle of the AO closed loop, $\mathbf{v}_t$ is a command vector of the one-previous cycle, α represent a closed-loop gain, $\mathbf{A}^+$ is the pseudoinverse matrix of an influence matrix and $\mathbf{s}_T$ is a slope vector obtained by the SHWS.

In addition, the wavefront aberration can be modulated by defining the target wavefront in the integral controller, which is described as

$$\mathbf{v}_{t+T} = \mathbf{v}_t - \alpha\mathbf{A}^+\left(\mathbf{s}_T - \mathbf{s}_{target}\right), \tag{1.12}$$

where $\mathbf{s}_{target}$ is the target slope vector. The residual wavefront will converge to the target wavefront, which is defined by the target slope vector $\mathbf{s}_{target}$.

1.4 Adaptive-optics retinal imaging

AO technology has been used to compensate the ocular monochromatic aberrations and enables high-resolution retinal imaging. Therefore, AO has been widely used in vision research and clinical applications [54–58].

High-resolution retinal imaging is realized by combining AO with several types of conventional retinal imaging devices such as a flood-illumination camera [10], scanning laser ophthalmoscopy (SLO) [59], and OCT [11–14]. These combined techniques successfully improved the lateral resolution of retinal images and provided cellular-level structural information of *in vivo* retina, such as photoreceptors, capillaries, and blood cells.

AO-SLO is a ultrahigh-resolution imaging system and enables *in vivo* cone and rod photoreceptor imaging [59–62]. AO-SLO has been also used for vascular imaging at the cellular level [63–68], which has enabled individual cell tracking including that of leukocytes and erythrocytes [63, 64, 66–68], and has enabled motion contrast to enhance the visibility of small retinal capillaries [65–67]. In addition, the use of offset pinhole aperture [69] improves retinal vascular imaging ability. The lateral resolution of AO-SLO is high enough to image all retinal capillaries, which are typically around 5 μm in diameter [7]. In addition, high-speed imaging suppress the involuntary motion artifacts.

AO-OCT is the state of art technology that allows *in vivo* microscopic investigation of the retina and choroid with extremely high lateral and axial resolution [11–14]. Thus, AO-OCT is capable of three-dimensional investigation of micrometer-scale structure, such as photoreceptors and capillaries. For instance, AO-OCT has been successfully used for *in vivo* three-dimensional photoreceptor imaging [70–72] and capillary imaging [73–76].

1.5 Overview

In this study, there are two main topics. At first, we developed AO-OCT using a 1-μm probe and demonstrated *in vivo* photoreceptor imaging. Second, several multiple-volume OCT-based angiographic algorithms have been used to enhance imaging ability of the capillary network.

In Chapter 2, the works for the development of 1-μm AO-OCT are described. We developed the system from the optical design. The system performance was evaluated numerically and experimentally. Furthermore, in order to extend the focal range, we created the spherical aberration on the pupil plane in addition to the cancellation of the ocular monochromatic aberration. The effect of spherical aberration was again evaluated numerically and experimentally. Finally, *in vivo* photoreceptor imaging performance was investigated. In total, four eyes of 4 subjects were examined. The image qualities were qualitatively and quantitatively assessed. A part of works was published in Optics Express [76–78] and Biomedical Optics Express [79].

In Chapter 3, the works of the multiple-volume OCT-based angiography are described. We used several type of angiographic algorithms to further enhance the vasculature image contrast with the helps of image-registration and averaging. We calculated averaged intensity, amplitude decorrelation, and averaged power of Doppler shift. For three-dimensional wide-field micro-vascular imaging, six eyes of 6 subjects were examined by a phase-stabilized swept-source OCT (SS-OCT). For high-resolution retinal and choroidal capillary imaging, four eyes of 4 subjects were examined by 1-μm AO-OCT. A part of works was published in Optics Express [76].

Chapter 2

Adaptive-optics OCT using one-micrometer wavelength probe

2.1 Introduction

The scattering and absorption property of the biological tissue depends on the wavelength of the light. For posterior-eye imaging, ophthalmic OCT typically uses a center wavelength of a 840-nm probe. This is mainly because of less water absorption and the affordability and availability of optical components. Hence, AO-OCT has been also developed for 840-nm wavelength band [11–14].

On the other hand, however, recent development of ophthalmic OCT has shown the enhanced image contrast at the deep region of the eyes using a 1-μm probe [15,30–33]. In addition, several types of high-speed swept laser source become available at 1-μm wavelength band [80–82]. Therefore, AO-OCT using a 1-μm probe (1-μm AO-OCT) is expected to be capable of high-resolution and high-speed posterior-eye imaging with high-penetration property.

To the best of our knowledge, we firstly developed 1-μm AO-OCT [78], though Mujat *et al.* has also demonstrated at nearly the same time [83]. In our laboratory, we started this work from the optical design, since AO system is required to be carefully designed (see Subsection 2.2.1). On the basis of this optical design, the optical system was carefully aligned and iteratively optimized to minimize an overall system aberrations. At the same time, the performance was evaluated numerically and experimentally. Then, the AO retinal scanner was combined with the previously-built spectral-domain OCT (SDOCT) [84]. Finally, *in vivo* photoreceptor imaging has been demonstrated (see subsection 2.2.4.3).

However, a larger probe beam diameter leads to the narrow depth of focus (DOF). This is problematic for *in vivo* AO-OCT imaging. For instance, the expected DOF is 52.7 μm with the beam diameter of 7.4 mm, and it is significantly smaller than the total thickness of the retina and choroid, which is around 0.6 mm. In addition, the temporal fluctuations make it difficult to maintain perfectly in-focus conditions. Hence, it is important to achieve a long focal range.

In order to extend the DOF while preserving the lateral resolution, there are several approaches such as three-dimensional scanning and point spread function engineering [85–

87]. As an example, an axicon lens was used to generate Bessel illumination for OCT imaging [88, 89].

Since the axicon lens can be considered to generate high-order spherical aberrations (SAs) [90], we hypothesized that a 3rd-order SA would extend the DOF of AO-OCT imaging. Thus, we intentionally create the 3rd-order SA on the pupil plane in addition to cancellation of ocular and system aberrations by modulating the wavefront aberration [79]. Then, the imaging performance and limitation of wavefront aberration modulation were investigated numerically and experimentally. Finally, *in vivo* photoreceptor imaging has been demonstrated with or without SAs (see Subsection 2.2.4.4).

2.2 Method

2.2.1 Optical design of adaptive-optics retinal scanner

In order to minimize the aberrations of AO retinal scanner, its optical setup was carefully designed using an optical design software (Zemax, Radiant Zemax, WA). The schematic diagram is shown in Fig. 2.1(a).

The probe beam is first collimated by an achromatic lens (L1), and expanded 1.5-times by a lens pair (L2 and L3). Here, the light passes an custom made achromatizer as described in Subsection 2.2.1.1. Then, the collimated light is reflected by a dichroic mirror, which reflects 1-μm light and transmits 700-nm. The reflected and transmitted light are transfered to the optically-conjugated planes: deformable mirror, horizontal and vertical scanners, and an eye pupil. Here, we employed a reflection-type configuration with off-axis relay optics using two spherical mirrors (SMs), as demonstrated as Roorda *et al.* [59]. This configuration suppresses the chromatic aberrations. Cumulative astigmatism originated from the horizontally off-axis SM pairs was canceled by cumulative astigmatism originated from a pair of vertically off-axis SMs (SM5 and SM6) [60]. The pair of vertically off-axis SM relays wavefront from the horizontal scanner to the vertical scanner and vice versa. The summary of the reflection-type configuration with off-axis relay optics is described in Table 2.1.

We placed a Badal optometer (L6 and L7) in front of the eye pupil to correct a large defocus of the eye, as demonstrated as Burns *et al.* [60]. The correctable range was from –9 D to 4 D, which covered more than 99% of the Asian population [91, 92]. In this Badal optometer, the off-axis configuration was used to reduce specular reflection.

The eye pupil is optically-conjugated to a plane of the lenslet array of the SHWS (Haso32, Imagine Eyes, Orsay, France), a reflective plane of a magnetic deformable mirror (Mirao52e, Imagine Eyes or High-speed DM97-15, ALPAO, France), and horizontal and vertical scanners. The retina is optically-conjugated to r_1, r_2, $\cdots$, r_6 and the fiber tip. The retinal and pupil magnification are summarized in Table 2.2.

The entire system was placed on a compact breadboard with an area of 750 $\times$ 900 mm^2.

Optical system performance Strehl ratio and footprint diagram were calculated to evaluate the monochromatic field aberration and on-pivot configuration. Here, we assumed

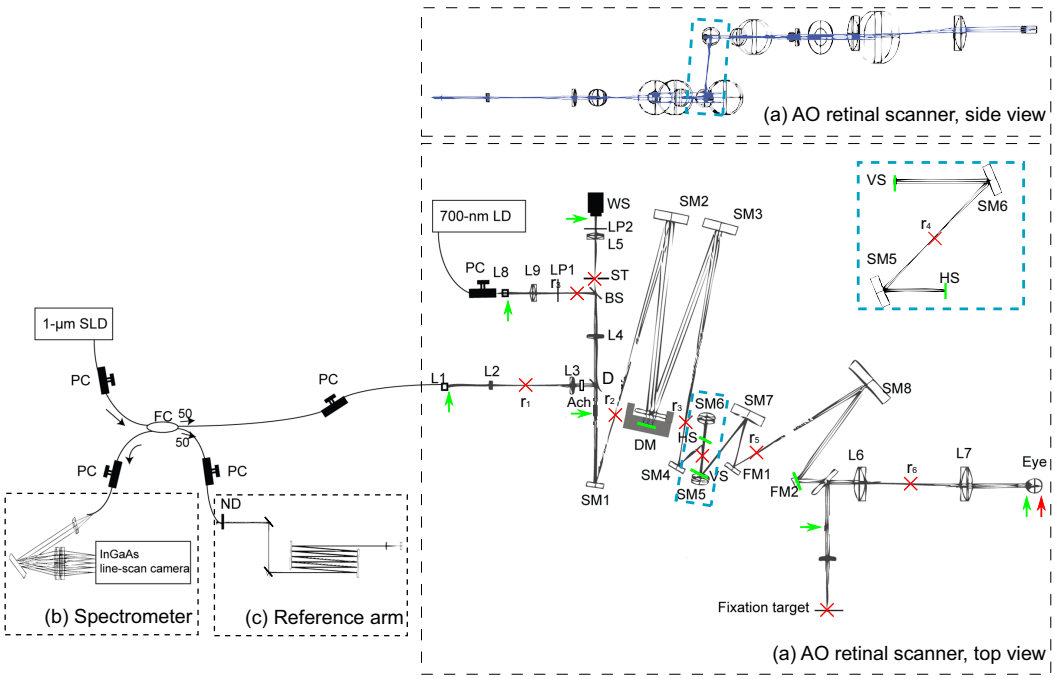

Figure 2.1: The schematic diagram of the optical setup of AO-SDOCT. PC: Polarization controller, FC: Fiber coupler, (a) The optical setup of the AO retinal scanner, L#: Lenses, LP#: Linear polarizers, D: Dichroic mirror, Ach: Achromatizer, ST: Stop, SM#: Spherical mirrors, FM#: Flat mirrors, WS: Wavefront sensor, DM: Deformable mirror, VS: Vertical galvanometric scanner, HS: Horizontal galvanometric scanner. The green bars and arrows indicate the optical conjugate planes of the pupil. The red crosses and arrow indicate the optical conjugate planes of the retina. $r_{\#}$: Optical conjugate planes of the retina. (b) Spectrometer. (c) Reference arm, ND: neutral density filter.

	Focal length [mm]	Deflection angle [degree]	Mirror size [mm]
SM1	101.6	θx = 8	ϕ25.4
SM2	304.8	θx = 5	ϕ50.8
DM	-	θx = 7	*ϕ15 or ϕ13.5
SM3	304.8	θx = 5	ϕ50.8
SM4	50.8	θx = 20	ϕ25.4
HS	-	θx = 22	4 (H) x 5 (V)
SM5	50.8	θy = 22.95	ϕ25.4
SM6	76.2	θy = 22.95	ϕ25.4
VS	-	θx = 16	24 (H) x 9 (V)
SM7	101.6	θx = 11.85	ϕ50.8
SM8	203.2	θx = 11.15	ϕ76.2

Table 2.1: Summary of the reflection-type configuration with off-axis relay optics. *: Clear aperture of Mirao52e and High-speed DM97, respectively.

Pupil magnification	Eye : HS : VS : DM : SHWS = 1 : 0.33 : 0.5 : 2 : 0.3
Retinal magnification	Fiber tip : r_1 : r_2 : r_3 : r_4 : r_5 : r_6: Retina = 1 : 6.25 : 8.47 : 8.47 : 8.47 : 11.29 : 4.45 : 0.928

Table 2.2: Pupil and retinal magnification

the monochromatic light source with a center wavelength of 1.02 μm. The intensity distribution is Gaussian apodization. For the simplicity, the Badal optometer (L6 and L7) and achromatizer were removed. Hence, the performance was evaluated at the surface of FM2. Strehl ratios over a 2 degree field of view (FOV) were calculated, as shown in Fig. 2.2(a). The results show that the Strehl ratios were larger than 0.91. It indicates the small field aberration and the cancellation of cumulative astigmatism. In addition, the pupil footprint was calculated, as shown in Fig. 2.2(b). The results show nearly perfect on-pivot configuration.

2.2.1.1 Achromatizer

A custom-designed broadband achromatizer is used. The general concept of an achromatizer was described by Fernández *et al.* [93]. We designed the achromatizer to cancel not only for the longitudinal chromatic aberration (LCA) of the eye but also for the LCA of the system. The optical design of the achromatizer is shown in Fig. 2.3(a). The numerical simulation showed the axial chromatic focal shift was corrected less than 3 μm at the wavelength bands of 970 nm and 1070 nm as shown in Fig. 2.3(b).

To cancel longitudinal chromatic aberrations of human eye, a custom-designed broad-

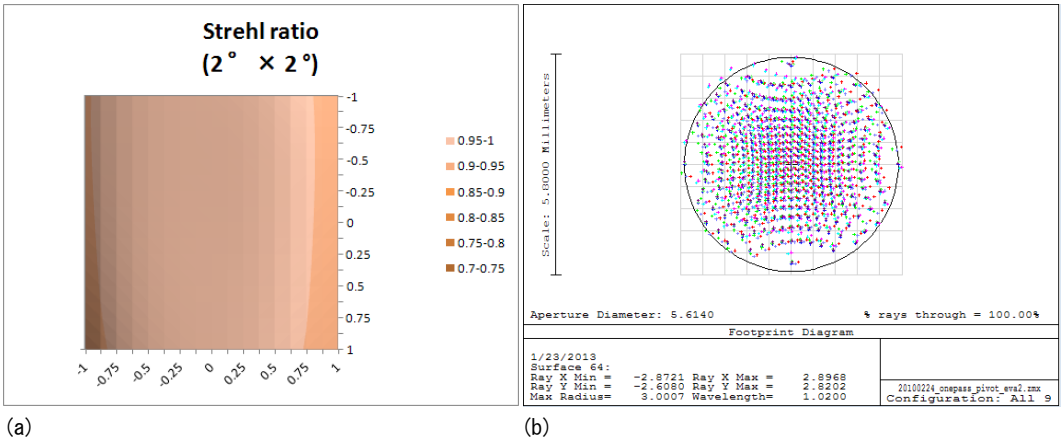

Figure 2.2: (a) Strehl ratios over 2 degreed FOV. (b) Pupil footprint diagram at FM2.

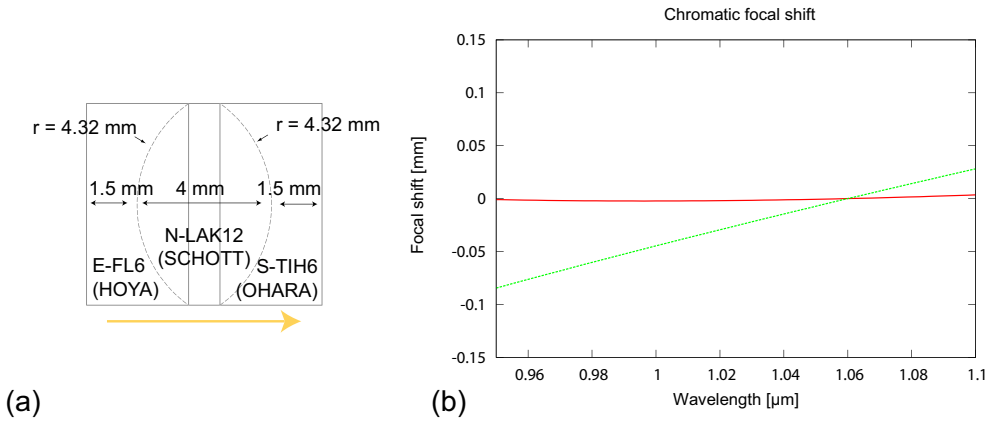

Figure 2.3: (a) Optical design of achromatizer. An yellow arrow indicates the beam direction from the fiber tip to the retina. (b) The chromatic focal shift with the achromatizer (red solid line) and without the achromatizer (green dashed line).

band achromatizer is used [93,94]. With this achromatizer, the axial chromatic focal shift was controlled to be less than 3 μm in the wavelength band of 970 to 1070 nm. The achromatizer is located between the input collimator and dichroic mirror which splits a back-scattered light to the fiber tip and to a wavefront sensor. This configuration prevents surface reflections from the achromatizer.

2.2.1.2 Scanning system

The AO retinal scanner has two galvanometric scanners to scan the beam over the retina. Here, we used them with a vertical-fast raster scanning protocol. The scanning FOV was calibrated by using an US Air Force test target (USAF 1951, CVI Melles Griot) that is placed at a retinal conjugated plane in a model eye, which comprised of a lens with a focal length of 16 mm.

2.2.1.3 Practical alignment

In practical alignment process, the SHWS was used to minimize the system aberrations. The wavefront aberrations were measured at each optically-conjugated plane, and the optical elements were adjusted. For the off-axis optics, the optical axes were first established by adjusting the angles of optics. And then, the defocus was minimized by adjusting the distance of SM pairs. However, it results in the change of its optical axis. Therefore, an iterative alignment process was necessary.

As an example, measured RMS wavefront errors for each optically-conjugated plane were 0.025 μm, 0.202 μm, 0.211 μm, and 0.130 μm at the position of the dichroic mirror, HS, VS, and FM2, respectively. Cancellation of the cumulative astigmatism was experimentally confirmed at the position of FM2, where the RMS errors was reduced from 0.211 μm to 0.130 μm. Here, it is noticeable that the beam diameter at FM2 is 2-times larger than the aperture of the SHWS, and the wavefront aberration measurement is relatively-inaccurate, though the SHWS can be used to minimize the low-order aberrations with the smaller aperture.

The measured beam diameter on the cornea was 7.4 mm, and it results in a transform limited $1/e^2$ beam width of 5.8 μm on the retina. The DOF, which is defined by 2-times Rayleigh length, was 52 μm.

The total optical loss of the AO retinal scanner was 2.8 dB for a single pass at 1 μm wavelength. This ensure that no vignetting was occurred. In addition, the measurable FOV was confirmed by applying the vertical and horizontal scanning, and it was approximately 2.5 degree (H) $\times$ 5 degree (V) FOV.

In order to have the on-pivot configuration, the optical conjugate plane of the pupil was confirmed by monitoring the scanning beam displacement. First, the DM was placed at the conjugation plane of HS. Here, the fiber collimator is placed after the HS, and hence the beam enters the system in an opposite direction. Then, the beam displacement was monitored on the reflective plane of the DM. The distance between DM and SM3 was adjusted. After the alignment of HS, the position of VS is placed at the optical conjugation plane of HS by adjusting the distance between VS and SM6. Here, the beam displacement was monitored at the plane of FM2. Hence, the iterative alignment process was necessary. Finally, the horizontal and vertical scanning pivot positions were confirmed by using the SHWS. The SHWS was placed at the position of the eye pupil and translated along the optical axis.

It is noted that the probe beam should be parallel to the beacon beam in our setup. Similarly, if the beam is aligned in opposite direction, the beam also should be parallel to the incident beam. Relative decenter and tip/tilt should be minimized. These misalignment results in the difference of cumulative wavefront aberrations between them, and the performance becomes unstable.

2.2.2 Adaptive-optics

2.2.2.1 Wavefront aberration measurement

The wavefront aberration was measured by SHWS (HASO32, Imagine Eyes) using a laser diode with a 700-nm center wavelength as a beacon (700-nm laser diode, HL7001MG, Thorlabs Inc., NJ). The specification of Haso32 is summarized in Table 2.3.

Since high-order aberrations over than 10th Zernike order is negligible with a pupil diameter of 7 mm [10], the required number of sub-apertures for 10th Zernike order is calculated as 66 (see Section 1.3). However, it is noticeable that the pupil is required to be more oversampled than this estimated number of sub-apertures, since the reliable maximum number of Zernike coefficients is degraded by several factors such as the effect of tear-film and pupil boundary errors. In our setup, the measured number of sub-apertures is typically over than > 300, when the eye pupil is dilated. It means that the pupil is oversampled 4-5 times than the required number of sub-apertures. The corresponding pupil diameter is 2.4 mm, which is mainly limited by the clear aperture of the DM and not by the eye pupil.

The specular reflections from the sample's surface and the surfaces of refractive-optics components overlapped the SHWS image and reduced the accuracy of wavefront aberration measurement. In order to avoid this problem, two linear polarizers (LP1 and LP2), whose orientations were orthogonal to each other, were placed after L9 and in front of the SHWS, respectively. In addition, a stop (ST) blocks the undesired stray light including the specular reflection, which is installed in front of L5, as shown in Fig.2.1.

In order to avoid the light integration of the SHWS during the pull-back action of the galvanometric scanner, the wavefront measurement is synchronized to vertical scan. Further, this scanning configuration reduces the speckles on the CCD camera [95] and hence the measurement become more stable. However, it should be noted that it is relevant only if the scanning FOV is within an isoplanatic patch [96].

2.2.2.2 AO beacon

A laser diode with a 700-nm wavelength was used as a beacon, though the probe beam is originated from a 1-μm SLD light source (Superlum diode, Ireland). This is because the 1-μm probe beam is not suitable for the ocular aberration measurement: the detector sensitivity of a silicon CCD is low at 1-μm wavelength, and higher depth penetration into the tissue results in relatively large depth scattered field of the SHWS image. In addition, the wavefront aberration measured by the beacon can be utilized effectively for the probe beam, since the wavefront measurement of the SHWS is basically achromatic and independent from the temporal coherence of the light source (see Section 1.3).

However, in practice, the longitudinal chromatic aberration (LCA) between the probe and beacon cause the difference of defocus of the eye, which is approximately 0.5 D [93], in addition to that of the refractive optics. It results in a longitudinal focal shift between the probe and beacon. In order to cancel the longitudinal focal shift, we adjusted the lens distance between the relay lens in front of the SHWS (L4 and L5). In addition, the residual chromatic aberration was canceled by applying an additional defocus to the target

Parameters	values
Aperture dimension	$3.6 \times 3.6\ mm^2$
Number of sub-apertures	32 (X) $\times$ 32 (Y)
Number of lens-let (N)	1024
Spatial resolution	$\sim 110\ \mu$m
Focal length of lens-let	5 mm
Diffraction limited FWHM of SHWS spot	$\sim$ 4.5 pixels
Number of pixels	492 (X) $\times$ 492 (Y)
Number of pixels/sub-apertures	$\sim$ 15 (X) $\times \sim$ 15 (Y)
Wavefront measurement accuracy	$< \lambda/100$
Maximum Zernike order	$\sim$ 10th order

Table 2.3: Specification of Haso32

Parameters	Mirao52e	High-speed DM-97
Number of actuators	52	97
Maximum wavefront (PV)	+/- 50 μm (tilt PV)	+/- 60 μm (tilt PV)
Mirror surface quality	0.006 μm RMS	$<$ 0.007 μm RMS
Effective diameter	15 mm	13.5 mm
Bandwidth	$>$ 200 Hz	$>$ 750 Hz

Table 2.4: Specifications of Mirao52e (Imagine Eyes) and High-speed DM-97 (ALPAO)

wavefront profile of an AO closed loop (see Subsection 2.2.2.4).

In order to extend DOF and reduce the double pass effect [60, 97], the smaller beam diameter was selected, which is 3.2 mm on the cornea.

2.2.2.3 Wavefront aberration correction

A magnetic deformable mirror (Mirao52e or High-speed DM97-15) was used to correct the measured wavefront aberrations. Mirao52e and High-speed DM97-5 were used in Subsections 2.2.4.4 and 2.2.4.3, respectively. The specifications of these deformable mirrors are described in Table 2.4. It should be noted that the reflected light have twofold aberrated wavefront than the deformed mirror surface. In other words, the wavefront quality is 2-times worse than the mirror surface quality.

The mirror shape was controlled by applying voltages for each actuator. The command vector was calculated by an integral controller as described in Section 1.3.

2.2.2.4 Adaptive-optics controller

The AO control software was implemented using LabVIEW SDK (Imagine Eyes). The standard integral controller was used (see Section 1.3). In order to obtain the influence matrix $\mathbf{A}$, positive and negative unit voltages were applied to each actuator of the DM,

and recorded slope vectors for each unit voltage. Note that the fiber collimator is placed at the position of the eye, and the beam enters the system in an opposite direction.

In the measurement, the AO closed loop was configured to have a gain of 0.3 or 0.4. Abnormal wavefront measurement values, which caused by the vignetting, blinking, or other factors, were rejected before the calculation of root-mean-square (RMS) wavefront errors and command voltages. The closed-loop was driven at a reputation frequency of 12 Hz.

The wavefront aberration modulation was realized by using the integral controller (Eq. (1.12)), any arbitrary wavefront can be set as a target wavefront and reconstructed by the AO closed-loop. However, in practice, its performance is limited by the fitting error. As described in Appendix, the achievable smallest residual wavefront error will be given by Eq. (4.6). Therefore, a large and high-order target aberration results in unavoidable large RMS error.

2.2.2.5 Extended depth of focus

In order to extend the DOF, we introduced a 3rd order SA by modulating the wavefront aberration [79]. Shortly, we intentionally create the SA on the pupil plane in addition to cancellation of ocular and system aberrations. As a result, a longitudinal aberration (LA) helps to extend the DOF.

In practice, the SA was required to be balanced by applying the additional defocus to shift the optimal focus position [79, 98]. We call this additional defocus as "counter defocus". In the geometrical optics, the minimum circle is positioned at 0.75 LA [98]. However, the optimal focus depends on not only the SA but also the intensity distribution on the pupil. In the numerical simulation, we found that the optimal focus was positioned at 0.25 LA. In the experiment, we found the counter defocus by recording the defocus coefficients, which provide the maximum OCT signal, for the every SAs (from -1.0 μm to 1.0 μm with 0.1-μm step). It was found that the counter defocus shift was closed to 0.25 LA as predicted by the numerical simulation.

Thus, the total amount of additional defocus coefficient was determined by the addition of the counter defocus and defocus cancellation of the residual LCA (see Subsection 2.2.2.2).

Numerical simulation In order to theoretically estimate the extension of DOF, we numerically simulated the polychromatic PSFs for SA = +0.4, 0.0, and -0.4 μm by using Zemax. In addition, in order to confirm the effect of chromatic aberrations, the numerical simulation was also performed with or without the achromatizer. Here, the Zemax model of the human eye is selected for the simplicity. The system and ocular aberrations are corrected by inserting the Zernike standard phase surface. The Strehl ratio was optimized larger than 0.99 at a center wavelength of 1020 nm. We calculated the theoretical depth-resolved PSF at each depth over +/- 1000 μm on the retina, where peak intensity reaches to maximum at the depth of 0 μm (counter defocus was considered). Here, it is noticeable that the counter defocus is no longer at 0.75 LA, but 0.25 LA due to the Gaussian apodization.

PSF was calculated based on the Huygens-Fresnel principle. We set the pupil and

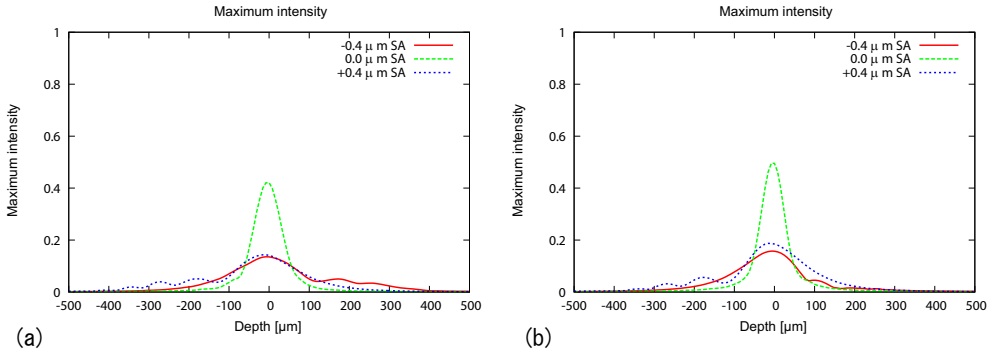

Figure 2.4: Peak intensity profiles for SA = +0.4, 0.0 and -0.4 μm without the achromatizer (a) and with the achromatizer (b).

image sampling sizes at 256 pix × 256 pix. The lateral spacing of the simulation was set at 0.5 μm. We calculated incoherence sum of the PSF at 5 difference wavelengths of 967 nm, 993 nm, 1020 nm, 1046 nm and 1073 nm, which were adopted as representative wavelengths of the broad band light source of a 1-μm SLD. The PSFs are divided by the peak intensity of diffraction limited PSF. The lateral resolution of the system was defined by $1/e^2$ beam width. The DOF was defined by the FWHM of central peak intensity profile along the depth.

In the case of SA = 0.0 μm (without SA), the profile of PSF was almost symmetric with respect to the focal plane as shown in Figs. 2.4. However, the depth profile of the PSF becomes asymmetric when SA was applied. When positive SA was applied, the transversal width of PSF was smaller at closer to the lens than farer from the lens, although some side peaks appeared. Wen negative SA was applied, the transversal width of PSF was smaller at farer from the lens than closer to the lens, and at the same time side peaks appeared. The DOFs with the achromatizer were 165 μm, 68 μm, 161 μm for SA = +0.4, 0.0, -0.4 μm, respectively. The DOF was extended 2.4 times with SAs. The $1/e^2$ beam widths with the achromatizer were 8 μm, 6 μm, 8 μm for SA = +0.4, 0.0, -0.4 μm, respectively. The lateral resolution becomes worse 1.3 times.

If we simply reduce the beam diameter to have an m-times longer DOF, we should shrink the beam diameter in $1/\sqrt{m}$ times. And hence, the lateral resolution is reduced in $\sqrt{m}$ times worse. Here, to have the same 2.4 times longer DOF, the lateral resolution should decrease in 1.55 times. It means that the lateral resolution is 1.2 times better with SA with the same DOF.

The effect of chromatic aberration in the DOF was significantly smaller than the the effect of the SA. In fact, the DOFs without the achromatizer were 176 μm, 80 μm, 186 μm for SA = +0.4, 0.0, -0.4 μm, respectively. This is approximately 1.2 times longer than that with the achromatizer, though the SA extends the DOF 2.4 times. In addition, there were no difference in lateral beam width in this numerical simulation. The peak intensity was slightly improved with achromatizer from 0.42 to 0.50. Thus, the achromatizer can be used to maximize the peak intensity and more effectively extend the DOF.

2.2.3 Spectral domain OCT

The SDOCT subsystem uses an SLD light source (Superlum diode, Ireland) with 1.02-μm center wavelength and a spectral bandwidth (FWHM) of 106 nm. The theoretical axial resolution is 4.7 μm in air and 3.4 μm in tissue.

Light from the source is divided and delivered to a sample arm and a reference arm by a 50/50 fiber coupler. In the sample arm, light is delivered to the retina via the AO retinal scanner. Backscattered light from the retina is recoupled into the fiber and sent back to the fiber coupler, where the backscattered light is recombined and interfered with the light from the reference arm.

The recombined light is delivered to the spectrometer, in which the light is collimated by an achromatic lens (AC254-050-B, Thorlabs Inc., NJ), diffracted by a reflective grating (GR50-1210, 1200 lp/mm, Thorlabs) and focused by a lens pair (AC508-050-B and AC508-150-B, Thorlabs) on an InGaAs 1024-pixel line-scan camera driven at a line rate of 91,911 lines/s (SUI1024LDH2, Sensors Unlimited Inc., NJ).

The sensitivity of the system was measured to be 81.5 dB with a sample power of 1.26 mW. Sensitivity was measured with a cat's eye consisting of an achromatic doublet (AC254-060-B, Thorlabs) and a mirror at an optical conjugated plane of the retina. Note that during this measurement the deformable mirror of the AO retinal scanner was flattened. This could result in underestimation of the sensitivity.

Alternatively, we also measured the sensitivity with aberration correction by an indirect method as follows. First, the system aberration was corrected with a model eye using a paper (scattering target) as a retina. Second, we replace the paper to a mirror (reflector) and realigned it. The defocus and tilts were adjusted to have the maximum re-coupling efficiency to the optical fiber of the interferometer. Finally, the sensitivity was measured. As a result, the sensitivity with aberration correction was 85.9 dB, which is 4.4 dB larger than the sensitivity without the aberration correction.

2.2.4 Measurement protocols

2.2.4.1 Subjects

As a static sample, a model eye was used to characterize the system performance. Here, the model eye comprised of a lens with a focal length of 16 mm or 30 mm and a paper (scattering) target which mimicked the refractive optics of the eye (cornea and crystalline lens) and retina, respectively.

For *in vivo* experiments, four eyes of 4 healthy subjects were examined in this study. The participants' characteristics are summarized in Table 2.5. Informed consents were obtained from all subjects. The protocol conformed to the Declaration of Helsinki, and it was approved by the Institutional Review Board of the University of Tsukuba. Prior to measurement sessions, two drops of 0.5% tropicamide and 0.5% phenylephrine were applied for pupil dilation and cycloplegia.

ID	Sph	Cyl	L/R	Axial eye length	Age
A	-7.3 D	-0.3 D	R	26.24 mm	26
B	-6.6 D	-0.4 D	R	27.52 mm	25
C	-1.2 D	-0.1 D	R	24.53 mm	32
D	-4.0 D	-0.3 D	R	25.73 mm	27

Table 2.5: Participants' characteristics. ID is the subject ID, Sph and Cyl are spherical and cylindrical refractive errors in diopters and L/R indicates the left (L)/right (R) eye.

2.2.4.2 Safety limit

The optical powers were 1.3 mW for the probing beam and 90 μW for the beacon beam. According to the safety limits defined by the American National Standard Institute [99], the maximum permissible radiant powers are 1.7 mW for the probing beam and 399μW for the beacon beam with an exposure time of 10 seconds, assuming the eye was illuminated by only one of the two beams. In order to account for the simultaneous multiple beam exposure, the total fractional powers respect to the maximum permissible radiant power should be less than 1.0. In our case, it was 1.3 mW/1.7 mW + 90μW/399μW = 0.99. And hence our measurement configuration satisfies the safety standard.

2.2.4.3 High-resolution OCT imaging

In order to experimentally evaluate the imaging performance of AO-OCT, the USAF test target was measured with or without AO. In addition, *in vivo* photoreceptor imaging has been demonstrated with AO.

Resolution target In the model eye experiment, the USAF test target was measured. First, the system aberration was corrected with the model eye, which comprised of a lens with a focal length of 16 mm. Second, we replace the paper to the USAF test target and realigned it to the focus plane. The defocus and tilts were carefully adjusted to have the maximum OCT signals, because the DOF is quite narrow. Here, we scanned 1 degree $\times$ 1 degree (235 μm $\times$ 235 μm, 512 pix $\times$ 512 pix) FOV.

***In vivo* photoreceptor imaging** In the human eye experiment, three eyes of 3 healthy subjects (A, C, and D) are examined. the eccentricity was set at from 1 to 5 degree Nasal. The imaged region on the retina was controlled by a fixation target, which was a grid pattern on a piece of paper. Volumetric measurements were performed at dimensions of 0.65 degree $\times$ 0.65 degree (128 $\times$ 128 A-lines). Nine sequential volumes were acquired at a speed of 5.6 volumes/s in a single dataset.

For the image comparison, we generated *en face* averaged projection images of the photoreceptor layer (PRL) with a projection thickness of 52 μm (21 pixels). The images were normalized by taking 0.1% and 99.7% percentiles. The outliers were forced to be zero

or 255. Here, the representative volumes which appeared with less involuntary eye motion artifacts are selected from the volumes taken at several datasets. Because the most severe reason for blurring image was the involuntary eye motion artifacts, the manual selection process was necessary.

2.2.4.4 Extended depth of focus

In order to experimentally evaluate the performance of 3rd-order SA, the ability of wavefront aberration modulation was first evaluated by a static model eye. The focal range with or without 3rd-order SA was evaluated by directly measuring the beam profile along the optical axis. Finally, *in vivo* photoreceptor imaging was demonstrated with or without SAs, and its performance was qualitatively and quantitatively evaluated.

Performance of wavefront aberration modulation In the model eye experiment, we measured the maximum OCT signals and the RMS wavefront error as altering the applied SA. The backscattered light from the thin paper target was recorded by OCT. The maximum OCT signal was defined as the average of maximum signals of 100 A-lines. The residual RMS wavefront errors were recorded by the wavefront sensor. The SA under consideration ranged from -1 μm to +1 μm with 0.1-μm step.

Beam profile measurement A scanning slit optical beam profiler (BP104-IR: Thorlabs) was employed in this study. However, the slit size is 2.5 μm, and the minimum measurable diameter for this beam profiler is 10 μm, which is significantly larger than the transform limited spot size of our standard model eye, 5.4 μm. Hence, we utilized another eye model with a lens with 30-mm focal length (AC127-030-B: Thorlabs) as an alternative.

In the experiment, we measured the intensity profile by the beam profiler at each depth. We set a target resolution at 1.2 μm. Note that intensity profile represents the integrated profile over the entire slit. After the acquisition, the measured intensity profiles were normalized at each depth location by the maximum intensity. This is because there was a significant intensity fluctuation by a rotational slit profiler at each depth. Then, we plotted the entire profiles for SA = +0.7, 0.0, and –0.7 μm. The measurement range was +/- 1000 μm with a 20-μm step, and the 0-μm depth was set so that the beam diameter reaches a minimum at this depth. The counter defocus obtained by another experiment was added for this measurement.

The variation of the lateral resolution as a function of the depth was then fitted to the following function, which is parameterized by w_0, w_0 and w_0:

$$w(z) = w_0\sqrt{1 + ((Z - Z_0)/z_R)^2} \tag{2.1}$$

where w_0 is the minimum lateral resolution, z is depth position, Z_0 is depth position with the minimum lateral resolution, and z_R is the Rayleigh length. $z_R$is used as a parameter to assess the focal range.

***In vivo* photoreceptor imaging with SA** In the human eye experiment, three eyes of 3 normal subjects (A, B, and C) were examined, whose demographics are summarized

in Table 2.5. The imaging region was set at 5 degree superior. In this study, we applied SA of +/- 0.4 μm and its associated counter defocus to have 3-times longer focal range (156 μm) in theory. This is because, in our case, the maximum applicable SA was 0.4 μm. In other words, AO-closed loop cannot converge with a target aberration larger than this maximum. Because there is the inevitable residual wavefront error discussed in Appendix. Here, the defocus was adjusted to focus on the photoreceptors.

Then, volumetric measurements were performed at dimensions of 0.8 degree $\times$ 0.8 degree (128 $\times$ 128 A-lines). Nine sequential volumes were acquired at a speed of 5.6 volumes/s in a single measurement session.

For the image comparison, we generated *en face* averaged projection images of the photoreceptor layer (PRL) with a projection thickness of 52 μm (21 pixels). The images were normalized by arbitrary taking maximum and minimum values to have a better image quality. The representative volumes which appeared with less involuntary eye motion artifacts are selected from the volumes taken at several measurement sessions. For the quantitative assessment of the image quality, we calculated the RMS value of *en face* projection image of PRL.

2.3 Results

2.3.1 High-resolution OCT imaging

2.3.1.1 Resolution target

The lateral resolution of OCT was improved with AO as shown in Fig. 2.5. The USAF test target with AO have a shaper image than that without AO. The estimated resolution was 181 lp/mm with AO (Group 7, Element 4, line width = 2.76 μm), and the theoretical resolution was 186 lp/mm, which line width is equal to the optical resolution 2.69 μm. Without the aberration correction, the RMS wavefront errors were typically 0.56 μm. With the aberration correction, the RMS wavefront errors were reduced to 0.01 μm, which was measured with a paper and before replacing it to the USAF test target.

However, it should be noted that there were subtle fluctuations in the galvanometric scanner and resulting in the lateral shifts in the images. In addition, the image was skewed due to the off-axis optics.

2.3.1.2 *In vivo* photoreceptor imaging

En face projection images of the photoreceptor layer (PRL) are shown in Figs. 2.6 and 2.7. Typically, measured RMS wavefront errors were ranged from 0.06 μm to 0.1 μm with AO, though the diffraction limited imaging is guaranteed less than 0.07 μm.

The photoreceptor images were clearly observed at 4 and 5 degree Nasal. However, photoreceptor cells are not clearly observed at more closer to the fovea, where cone-photoreceptor cells are more densely packed [100].

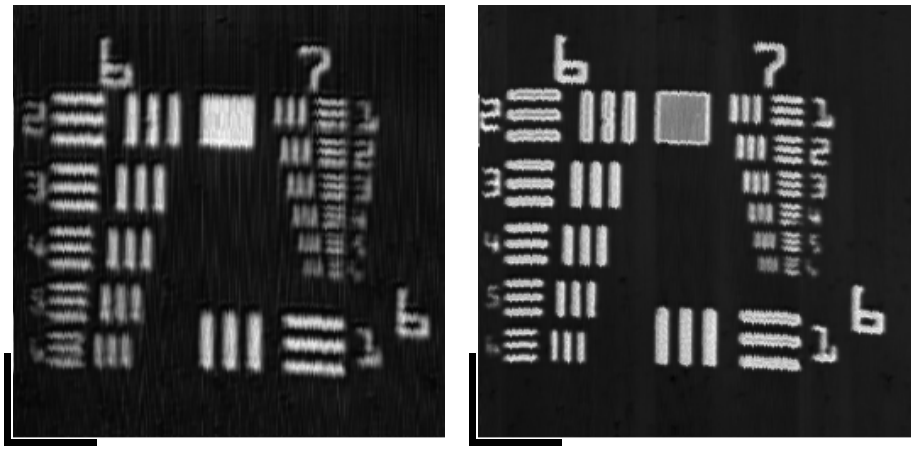

Figure 2.5: (a) The USAF test target without AO. (b) The USAF test target with AO. The measured FOV is 235μm $\times$ 235 μm. The black bars indicate 50 μm.

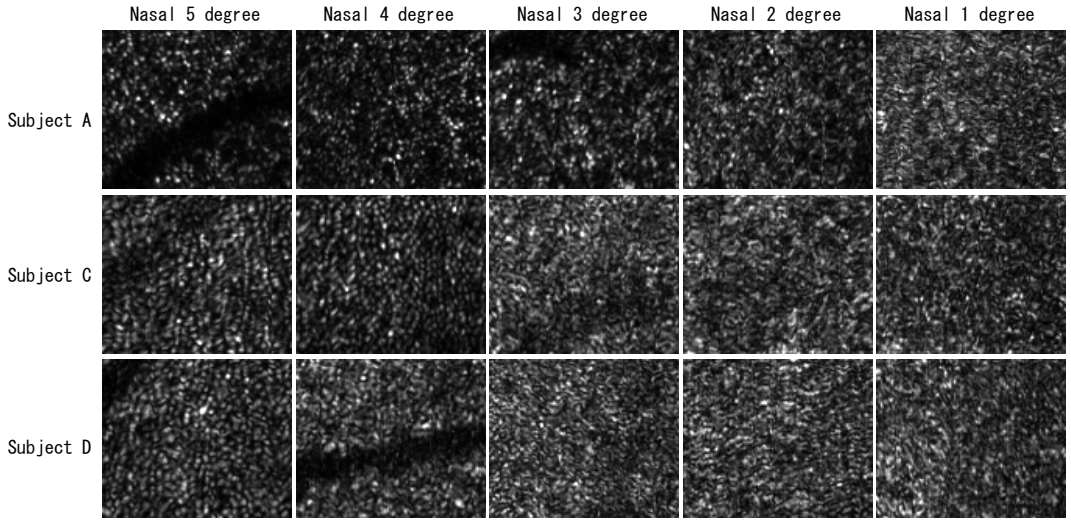

Figure 2.6: Photoreceptor images in linear scale. The FOV is 0.62 degree (H) $\times$ 0.52 degree (V).

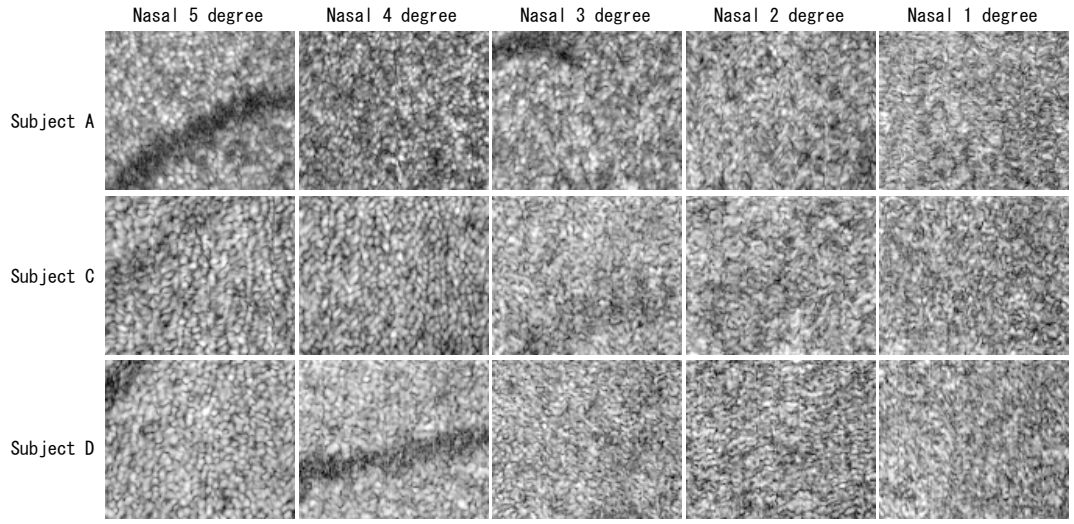

Figure 2.7: Photoreceptor images in logarithmic scale. The FOV is 0.62 degree (H) × 0.52 degree (V).

2.3.2 Extended depth of focus

2.3.2.1 Performance of wavefront aberration modulation

The maximum OCT signals are plotted as a function of applied SA, as shown in Fig. 2.8(a). The maximum OCT signal was found at SA of around 0.0 to 0.1 μm. The possible reason of the tiny positive shift would be the system induced SA originated from the detection path and/or wavelength differences between the probe and beacon beams. The residual RMS error was increased as a function of the coefficients of applied SA, as shown in Fig. 2.8(b). Numerical simulation results showed the similar tendency with the experimental results. The discrepancy between the experiment and simulation would be explained by measurement error which did not take into account in the simulation (see Appendix).

2.3.2.2 Beam profile measurement

We compared the transversal intensity profiles in cross section at several depths, as shown in Fig. 2.9. When positive SA was applied, the transversal width of intensity profile was smaller at closer to the lens. When negative SA was applied, the transversal width of intensity profile was smaller at father from the lens. The estimated z_R were 172 μm, 126 μm, and 173 μm for SA = +0.7, 0.0, and –0.7 μm, respectively. The DOF was extended 1.4 times with SAs. Both of positive and negative SAs showed the extension of focal range. The minimum lateral resolutions w_0 were 16.6 μm, 14.2 μm, and 16.2 μm for SA = +0.7, 0.0, and –0.7 μm, respectively. The lateral resolution would become worse 1.2 times with SAs.

These results indicate first that the effective focal range can be extended by applying SA. Second, lateral resolution was well preserved with SAs.

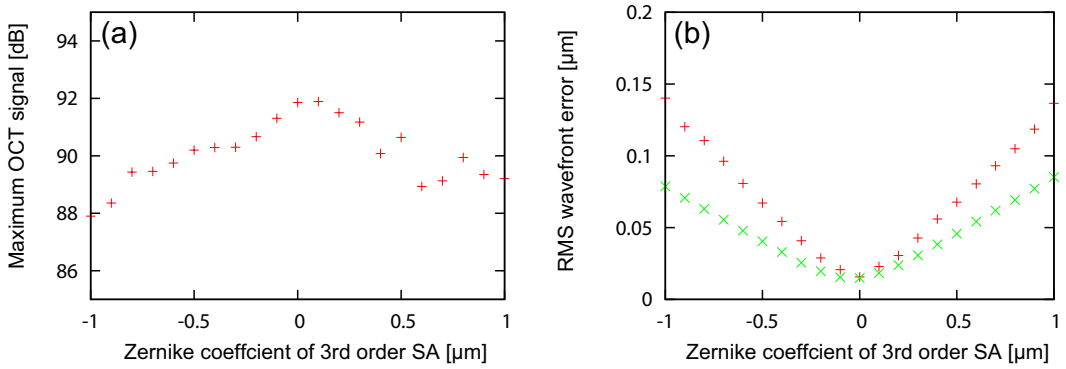

Figure 2.8: The maximum OCT signals for each SA is shown in (a). The RMS wavefront errors for each SA is shown in (b). The "+" and "×" dots indicate the experimental and simulation results, respectively.

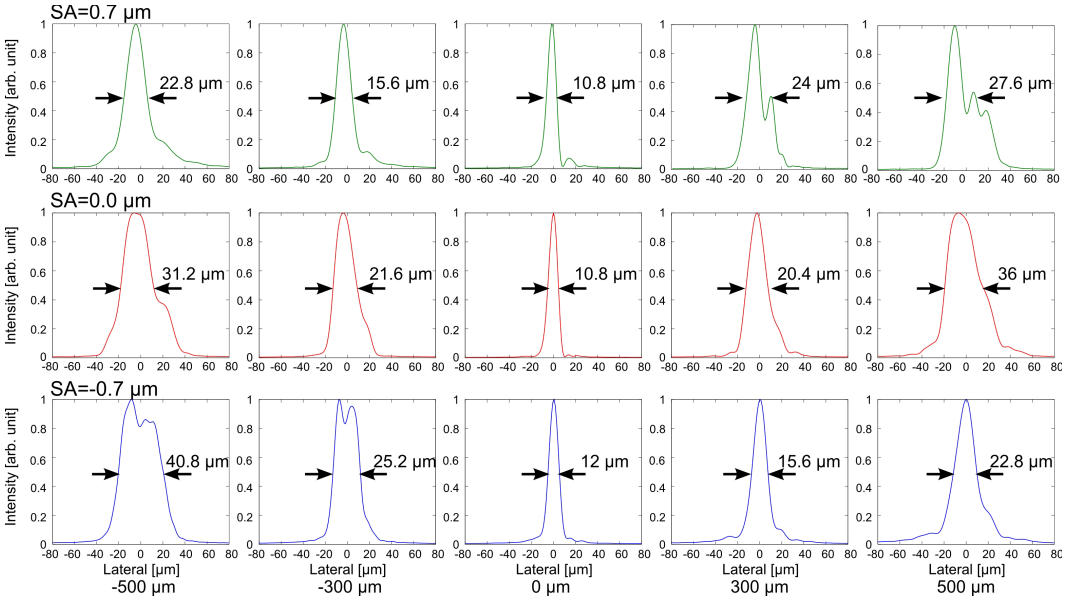

Figure 2.9: Normalized intensity profiles for SA = +0.7, 0.0, and –0.7 μm in linear scale. The Black arrows and numbers indicate the full width at half-maximum (FWHM).

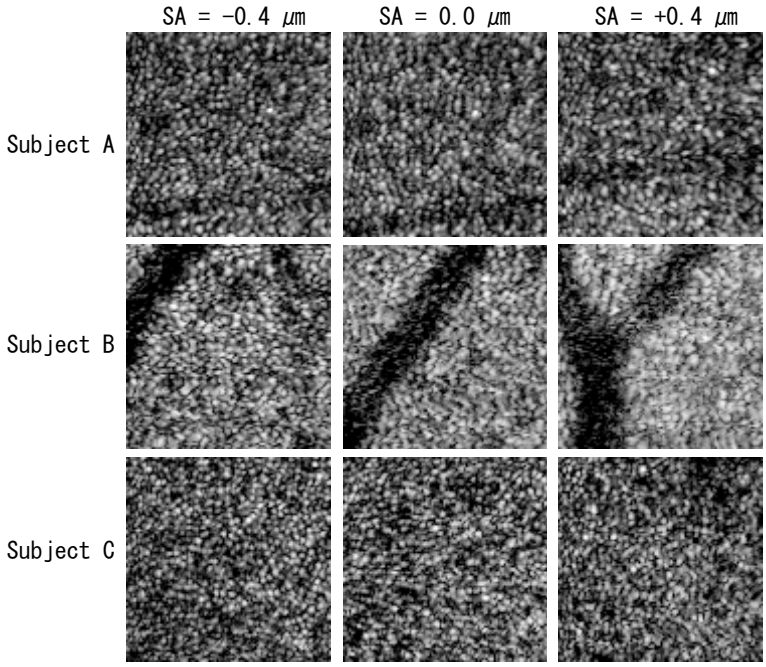

Figure 2.10: *En face* projection images on PRL of Subject A, B and C are shown in the first, second and third row, respectively. Images in the first, second and third columns are taken with +0.4-μm SA, 0.0-μm SA, and -0.4-μm SA, respectively. FOV of cropped images was 0.64 degree $\times$ 0.64 degree (102 pixels $\times$ 102 pixels).

2.3.2.3 *In vivo* photoreceptor imaging with SA

Figure 2.10 shows *en face* projection images of the PRL. We qualitatively observed better image quality with -0.4-μm SA for all subjects than 0-μm or +0.4-μm SA. To more quantify the image, RMS of the image, i.e. the mean signal energy of the image was obtained. Comparable or higher RMS values were found with -0.4-μm SA than without SA as shown in Fig. 2.10. The image quality with +0.4-μm SA was worse than the others. The residual RMS wavefront errors for each SA are shown in Fig. 2.11(b). Without SA, RMS wavefront errors were less than 0.1 μm for all subjects. Introduction of SA increases the RMS error up to around 0.16 μm (results ranged from 0.1 μm to 0.16 μm). Despite this increasing RMS error, we also found that the image quality for all subjects was better or comparable with -0.4-μm SA than without SA.

2.4 Discussions

2.4.1 *In vivo* photoreceptor imaging

Although the lateral resolution was improved with AO as shown in Figs. 2.5, almost of cone-photoreceptor cells were not well observed especially at closed to the fovea, which were clearly observed with 840-nm AO-SLO and AO-OCT systems [59, 61, 72].

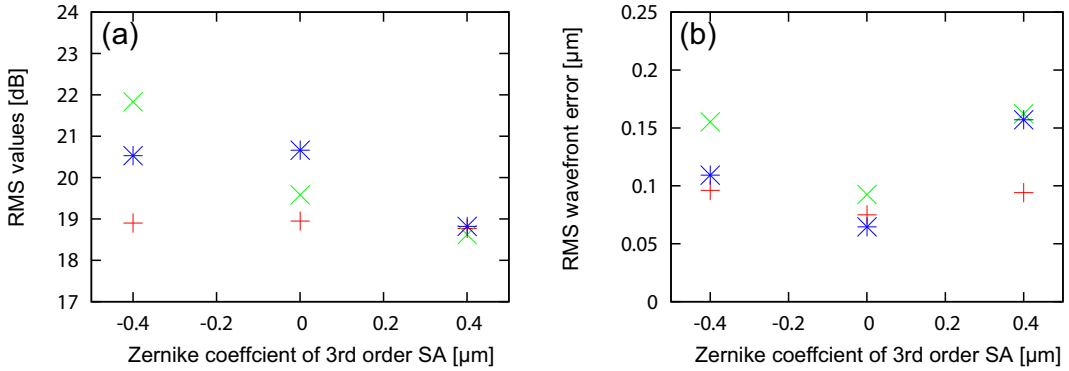

Figure 2.11: RMS values of *en face* projection images for SA = +0.4, 0.0 and -0.4 μm are shown in (a). Residual RMS wavefront errors for = +0.4, 0.0 and -0.4 μm are shown in (b). The "+", "×", and "*" indicate subject-A, -B, and-C, respectively.

For the retinal imaging, the involuntary eye motion artifacts were the most severe problem, and they are random and not predictable. Hence, it is difficult to discriminate between the effects of involuntary motion artifacts from the other factors: residual aberrations, wavelength dependent contrast [101], structural differences including the axial eye length, system imperfection and so on. Nor surprisingly, in order to quantitatively analyze the individual photoreceptor cells, the current imaging speed (5.6 volumes/sec) is insufficient. More faster image acquisition is necessary. High-speed OCT imaging technology [81, 82] would overcome this issue.

2.4.2 Extended depth of focus

2.4.2.1 *In vivo* photoreceptor imaging with SA

Through the measurement, we qualitatively and quantitatively observed the equivalent or higher contrast of cone mosaic with 0.4-μm SA than without SA, though there were no statistically significant differences. The reasons would be explained by the larger fluctuation of the OCT signal intensity than the effect of SA. For instance, the OCT signal intensity gain with SA was found only 1–2 dB in the phantom imaging. However, for the human retinal imaging, there are large fluctuations from the other factors: involuntary motion artifacts, structural changes, and OCT signal decay. More details analysis of the effect of SA apart from other factors based on larger population would be a future study.

2.4.2.2 Benefit for retinal imaging

Proper alignment of the depth position of the focus is essential for high contrast imaging. There are several uncontrollable factors in this alignment. For instance, multi-layer structures in the retina cause a relatively large depth scattered field of a wavefront sensor images, hence the exact depth position of wavefront sensing is not predictable. In addition, micro-fluctuations of the accommodation also result in fluctuations in the depth position of the reference of the wavefront measurement [95, 102].

Involuntary eye motion could also be a cause of turbulence. In AO retinal imaging, the depth position of the focus is aligned based on an *en face* image. This maneuver is easy and practical for AOSLO and a flood illumination AO fundus camera. However, it is not totally compatible with AOOCT because AOOCT, with the exception of T-scan time domain AOOCT, required a full volumetric acquisition to obtain an *en face* image. In this circumstance, a long focal range obtained by intentionally induced SA becomes beneficial. This benefit might be resulted in the slight differences of image contrast were observed among several SA values as mentioned in Subsection 2.3.2.3.

2.5 Summary

In summary, we successfully enhance the lateral resolution of ophthalmic OCT by developing 1-μm AO-OCT from the optical design. *In vivo* photoreceptor cells were resolved at 4–5 degree Nasal, which were rarely observed without AO.

In addition, we further enhance the imaging ability of AO-OCT by modulating the wavefront aberrations. Here, we introduced the SA to extend the DOF of AO-OCT. Although experimental results of the model eye indicate the extension of DOF, the evident difference was not observed in *in vivo* photoreceptor images. We only qualitatively found that the negative-SA of 0.4 μm in RMS provides slight better image contrast than non-and positive-SA of 0.4 μm in RMS.

Chapter 3

High-contrast micro-vascular imaging

3.1 Introduction

Abnormal vascular network disturbs our visual function [7, 103–106]. Hence, the vascular imaging is an important for the diagnosis in the field of ophthalmology. Especially, the capillaries have an unique function to directly exchange the oxygen, nutrients, carbon dioxide, and cellular waste products with the surrounding tissues. Therefore, the capillary imaging is one of the important keys for the better diagnosis.

Several OCT-based angiographic methods were successfully used for a non-invasive three-dimensional micro-vascular imaging [15–29], Nowadays, these techniques have been utilized for the detection of abnormal blood vessels [107].

However, the image quality of the OCT-based angiography is limited by the involuntary motion artifacts and low signal to noise ratio (SNR). In addition, the capillary have a small diameter of 5-μm [7]. Therefore, the capillary flow velocity is slow and approximately 1–3 mm/s [105, 108]. Hence, high-resolution and high-sensitive methods are required.

In this study, we used multiple-volumes to further enhance the vasculature contrast of several OCT-based angiographic methods (see Section 3.2.1). Here, we calculated averaged intensity, amplitude decorrelation, and averaged power of Doppler shift. Then, three-dimensional retinal and choroidal micro-vascular imaging has been demonstrated using a phase-stabilized swept-source OCT (SS-OCT) and 1-μm AO-OCT as described in Subsections 3.3.1 and 3.3.2, respectively.

3.2 Method

3.2.1 OCT-based angiographic method

3.2.1.1 Image registration

Since multiple volumes are taken at a single retinal location, the volumes are registered to each other semi-automatically.

Shortly, first the axial motions along slow-scan are corrected by taking cross-correlation coefficients between neighboring A-scans. Here, we used averaged displacements along slow-scans. This enables smooth flattening. Second, the axial motions along fast-scan, mainly tilt, are corrected by cross-correlation. Here, we used averaged displacements along fast-scans. Then, each volume are flattened. Here, the depth position of each volume is detected by employing customized edge detection and an iterative smoothing algorithm.

The transversal shifts among volumes are detected and corrected using a phase correlation based registration algorithm. In detail, *en face* slices of photoreceptors are extracted from each volume. Then, the *en face* images are segmented into several strips along the fast-scan axis. The transversal motion of the strips relative to a proper reference image is detected by the phase-correlation based registration algorithm. Some segmented strips with small correlation coefficients are rejected. Finally, a set of motion-corrected volumes is obtained.

3.2.1.2 Multiple-volume OCT-based angiographic algorithms

After the image registration, set of B-scans taken at the same location but in different volumes are averaged with a certain inclusion criteria. In this study, e used intensity averaging (averaged intensity, Eq. (3.1)), amplitude decorrelation (amplitude decorrelation, Eq. (3.2)), and weighted averaged Doppler power (averaged Doppler, Eq. (3.3)).

Averaged intensity The averaged intensity represents the axial profile of backscattering light from the sample as described as

$$\log\left(\bar{I}\right) = \log\left(\frac{\sum_{n=1}^{N} I_n\left(x,y,z\right) T_n(y)}{\sum_{n=1}^{N} T_n(y)}\right), \tag{3.1}$$

where N is the number of volumes utilized.

Amplitude decorrelation The amplitude decorrelation represents the amplitude fluctuation during fixed time interval [28, 29], which is defined by the number of A-scans per B-scan. Hence, the amplitude decorrelation is independent from the phase fluctuation and derived only from scattering information of OCT signals. The amplitude correlation coefficient is given by $\rho_{amp} = \dfrac{\mathbf{E}[|\Gamma_i(z,t)||\Gamma^*_{i+1}(z,t+\Delta t)|]}{\mathbf{E}[|\Gamma_i(z,t)|^2]}$. Here, the expected value can be calculated by averaging them with certain threshold, which is described as

$$\sigma^2_{Amp.Decorr.B-B} = 1 - \frac{\sum_{n=1}^{N}\left(\sum_{m=1}^{M}|\Gamma_m||\Gamma^*_{m+1}|\right) T_n(y)T'_n(x,y,z)}{\sum_{n=1}^{N}\left(\sum_{m=1}^{M}\left(\frac{I_m+I_{m+1}}{2}\right)\right) T_n(y)T'_n(x,y,z)}, \tag{3.2}$$

T is a $0,1$ function which takes zero if the corresponding OCT B-scan frame failed the volume registration, and hence only B-scans in volumes which were successfully co-registered with the other volumes were utilized for the calculation. $T'_{\rho_{amp}}$ is also a $0,1$ function which takes zero if the magnitude of correlation function of corresponding pixel from the noise

floor $10 \log \frac{\sum_{m=1}^{M} |\Gamma_m(\mathbf{r})\Gamma^*_{m+1}(\mathbf{r})|}{M\sigma^2}$ is less than 10 dB. M is the number of B-scans to be averaged and the superscript * denotes the complex conjugate. If $\sum_{n=1}^{N} TT' \leq 1$, the result is set to be zero.

Averaged Doppler The averaged Doppler represents the amount of phase-shift caused by moving scatterers during fixed time interval, which is again defined by the number of A-scans per B-scans [20–22, 46]. Hence, it requires high phase-stability and bulk motion correction. The weighted averaged of Doppler power is described as

$$\overline{\Delta\phi^2_{B-B}} = \frac{\sum_{n=1}^{N} \left(Arg \left(\sum_{m=1}^{M} \Gamma_{m,n} \Gamma^*_{m+1,n} \right) \right)^2 T_n(y) T'_n(x,y,z)}{\sum_{n=1}^{N} T_n(y) T'_n(x,y,z)}, \tag{3.3}$$

where $\Delta\phi_{B-B}$ is the phase-difference between OCT B-scans after the bulk motion correction, which is described in the following paragraph. If $\sum_{n=1}^{N} TT' \leq 1$, the result is set to be zero.

A constant phase offset ϕ_{bulk} owing to sample bulk motion and unstable scanning, disturbs the Doppler measurement. Methods that use the mode or mean of the Doppler shift to detect and cancel the bulk motion have been demonstrated [45, 109–111].

However, with the long time separation such as that in our protocol, many small capillaries can be detected, and hence the static regions become small. This disturbs the above-mentioned standard methods for bulk motion correction. This is because the detection accuracy of the constant phase offset relies on the selection of the static tissues. In other words, by selecting the static regions effectively, we can improve the estimation accuracy. Here, we used the OCT signal intensity as a weight function to effectively select the static tissue [45]. In addition, this estimator was extended into a complex form to have higher robustness. The weight function provides an appropriate selection of the static tissues of the eye for the following reasons. First, the OCT signal is, in SD-OCT, weaker in a dynamic region with stronger motion, such as in blood vessels [41, 112]. Second, the static retinal structures including photoreceptors, the retinal pigment epithelium (RPE), and nerve fiber layers are strong scatterers and hence have high OCT signal intensity. For instance, the photoreceptors and RPE typically have a mean signal-to-noise ratio (SNR) larger than 20 dB, while the choroid and retinal capillaries has an SNR of around 15 dB or less. Third, because the random phase noise depends on the SNR [113], the phase value is more reliable with the higher SNR. Under the above circumstances, the intensity-weighted mean estimator is a good candidate for the bulk motion correction.

Another problem associated with the Doppler measurement protocol using a long time separation is frequent phase wrapping. This is because the measurable maximum Doppler velocity is small. Although this is not problematic in the case of the mode estimator [109], the phase wrapping disturbs the mean estimation [45] and it should be corrected by some means. And hence, in this paper, we calculated the mean value in complex form, because this complex mean is robust for the phase wrapping.

We used a mean estimator, which is described as

$$\phi_{bulk} = Arg[\sum_{j} \Gamma_i(j)\Gamma^*_{i+1}(j)], \tag{3.4}$$

ϕ_{bulk} is the estimated sample bulk motion, $\Gamma(j)$ is the complex OCT signal at the j-th depth pixel in the i-th A-line. It is noteworthy that the amplitude of $\Gamma_i(j)\Gamma^*_{i+1}(j)$ is used as a weight of this mean calculation. This weight takes a larger value for a stronger OCT signal. This is equivalent to a part of bulk motion correction as proposed by Lee *et al.* [114], which is called as an axial global phase fluctuations.

This proposed method has additional advantages other than the robustness to the phase wrapping occurred by a large bulk motion. First, the estimation is robust even in the case with large blood vessels, in which the blood flow velocity far exceeds the maximum velocity range. Since, in such large blood vessels, the phase values appear as random values with a zero-mean, the complex mean estimator is less sensitive to the blood flow but selectively sensitive to the bulk motion of the eye. Second, it is significantly faster in computation than the mode estimator and the other recently proposed iterative methods [21, 22, 109]. Third, it does not need to apply intensity threshold, and hence is a totally linear operation [111].

In order to reduce the noise, several number of B-scans are averaged form for the averaged Doppler and amplitude decorrelation (see Eqs.(3.2) and (3.3)). In Subsection 3.3.1.1, the number of averaged B-scans M is set to 6. In Subsection 3.3.2.3, M is set to 3. However, in Subsections 3.3.2.1 and 3.3.2.2, the B-scans were not averaged.

3.2.1.3 *En face* projection

To generate *en face* projections, we first segmented the retina and choroid into several layers by employing a customized algorithm for edge detection and smoothing. The following layer interfaces are automatically or manually segmented; i.e., the interface between the inner limiting membrane and nerve fiber layer (ILM/NFL), the interface between the NFL and ganglion cell layer (NFL/GCL), the interface between the inner plexiform layer and INL (IPL/INL), the interface between the inner nuclear layer and the outer plexiform layer (INL/OPL), the interface between inner and outer segment of photoreceptor (IS/OS) and the interface between the retinal pigment epithelium and choroid (RPE/choroid).

In Section 3.3.1, the following *en face* projections are generated. In the retina, we generate *en face* projections of two retinal layers, which are denoted as Retinal and INL projections, on the basis of the segmentation. Here, Retinal projection is generated by integrating 50 pixels (182 μm in tissue), which includes almost all of the retina. INL projection is generated by integrating 20 pixels (72 μm in tissue), which includes almost all of INL. In the choroid, we generate *en face* projections of two independent layers, which are denoted as projections Ch1 and Ch2. These projections are segmented and numbered from the RPE/Choroid interface, and the thickness of each projection is seven pixels (26 μm in tissue). To enhance the image contrast and ignore the outliers, the projection images of the averaged intensity and averaged Doppler images were normalized by taking

ID	Sph	Cyl	L/R	Axial eye length	Age
A	-5.6 D	-1.0 D	R	26.88 mm	37
B	0 D	-3 D	R	23.49 mm	32
C	-7.3 D	-0.3 D	R	26.24 mm	26
D	-1.2 D	-0.1 D	R	24.53 mm	32
E	-4.0 D	-0.3 D	R	25.73 mm	27
F	-6.2 D	-0.2 D	R	25.7 mm	30

Table 3.1: Participants' characteristics. ID is the subject ID, Sph and Cyl are spherical and cylindrical refractive errors in diopters and L/R indicates the left (L)/right (R) eye.

0.1% and 99.7% percentiles, though that of the amplitude decorrelation was normalized by taking 20% and 99.7% percentiles. These parameters are empirically determined.

In Section 3.3.2, the following *en face* projections are generated. In the retina, on the basis of the segmentation, we generate *en face* projections of four independent retinal layers, which are denoted as an NFL, GCL+IPL, IPL/INL, and INL/OPL projections. In the choroid, we generate *en face* projections of four independent choroidal layers, which are denoted as projections CC1 to CC4. These projections are segmented and numbered from the RPE/choroid interface, and the thicknesses of each projection is three pixels (7.4 μm in tissue) in Section 3.3.2.1, and four pixels (9.9 μm in tissue) in Section 3.3.2.2.

In order to further denoise the *en face* projections of vascular images, a transversal moving average filter was applied with kernel size of 3 pix (4.5 μm, fast) $\times$ 3 pix (4.5 μm, slow) in Sections 3.3.2.1, and 3 pix (4.5 μm, fast) $\times$ 5 pix (3.8 μm, slow) in Section 3.3.2.3. Further, the projection images of the averaged intensity and averaged Doppler images was normalized by taking 0.1% and 99.9% percentiles, though that of the amplitude decorrelation was normalized by taking 15% and 99.9% percentiles. These parameters are empirically determined.

On the other hand, no moving average filter was applied in Section 3.3.2.2. All projection images were normalized by taking 0.1% and 99.9% percentiles.

3.2.2 Measurement protocols

Six eyes of 6 healthy subjects are involved in this study. The participants' characteristics are summarized in Table 1.1. Informed consent was obtained from all subjects. The protocol conformed to the Declaration of Helsinki, and it was approved by the Institutional Review Board of the University of Tsukuba.

In this study, we first demonstrated *in vivo* micro-vascular imaging by SS-OCT. The measurement protocols are described in Section 3.2.2.1. Next, we demonstrated *in vivo* capillary imaging by using the 1-μm AO-OCT, which is previously described in Chapter 2. The measurement protocols are described in Section 3.2.2.2.

3.2.2.1 *In vivo* micro-vascular imaging by SS-OCT

In Section 3.3.1.1, to investigate the general trend of multiple-volume OCT-based angiographic algorithms, six eyes of 6 subjects were examined by SS-OCT [22]. No eye-drops were applied before the measurement. The macular region was measured with the scanning protocol D, as described in Table 2.1. Since it has a standard imaging resolution, the imaging field of view (FOV) is much wider than the that of AO-OCT, as shown in Fig. 3.1. Ten volumes were acquired separately, and five representative volumes were used to generate the OCT-based angiographic images: averaged intensity, amplitude decorrelation, and averaged Doppler (Eqs. (3.1), (3.2) and (3.3)).

Phase-stabilized swept-source OCT In order to have a wide FOV and standard non-AO imaging resolution, we used a custom built swept-source optical coherence tomography (SS-OCT) for this study, which have several advantages for the retinal and choroidal imaging in terms of high-penetration, high-speed, and low signal roll-off. The details of the system are described in Ref. [22].

Shortly, SS-OCT uses an 1-μm swept laser source (Axsun Technologies Inc., MA) with center wavelength of 1060 nm, a spectral bandwidth of 100 nm, and a scanning speed of 100,000 A-scans/s. Light from the source passes through a polarization controller and a polarization independent circulator. Then, the light from the source is divided and delivered to a sample arm and a reference arm by a 50/50 filter coupler. Backscattered light from the retina is recoupled into the fiber and sent back to the filter coupler, where the backscattered light is recombined and interfered with the light from the reference arm. The recombined light is detected by balanced photodetector (PDB130C, Thorlabs Inc.). The measured depth resolution was (-6dB width) 11.0 μm in air and 8.0 μm in tissue. The optical power on the cornea were 1.85 mW, which is below the safety limits defined by the American National Standard Institute.

In order to measure Doppler phase-shift correctly, phase changes due to spectral shift and bulk motion were numerically corrected by using a two step algorithm [22]. Then, it enables significant improvement of *in vivo* Doppler measurement.

3.2.2.2 *In vivo* capillary imaging by AO-OCT

In Section 3.3.2, prior to measurement sessions, two drops of 0.5% tropicamide and 0.5% phenylephrine were applied for pupil dilation and cycloplegia. Three types of scanning protocols A-C were used, as described in Table 2.1.

In Subsection 3.3.2.1, to show the application of depth-resolved capillary imaging by 1-μm AO-OCT, we scanned subject A with scanning protocol A. Nine sequential volumes were acquired at a speed of 5.6 volumes/s in a single measurement data set and were used to generate the averaged intensity and averaged Doppler projections (Eqs.(3.1) and (3.3)). The eccentricity was set to be 3.0-degree inferior and 1.5-degree nasal.

In Subsection 3.3.2.2, to show a potential to image choriocapillaris by 1-μm AO-OCT, we scanned subject B with the scanning protocol C. Because of larger FOV and more dense sampling, it requires long measurement time and results in larger involuntary motion artifacts. Hence, only a single volume was obtained by chance. Intensity, power of

Protocol ID	Image size [pix] (fast × slow)	FOV [degree] (fast × slow)	Speed [vol/s]	N	$\frac{\delta_x}{d_{width}}$	Min. velocity [mm/s]
A	128 × 128	0.65 × 0.65	5.6	9	0.25	0.029
B	256 × 512	1 × 1	0.7	1	0.097	0.010
C	128 × 256	0.65 × 0.65	2.8	5	0.13	0.023
D	128 × 1024	5 × 5	0.7	5	0.22	0.013

Table 3.2: Summary of scanning protocols. The fractional displacement $\frac{\delta_x}{d_{width}}$ is the separation between adjacent B-scans with respect to the $1/e^2$ beam diameter of the probe. N is the total number of volume in a dataset. The minimum velocity is estimated for an SNR of 20 dB.

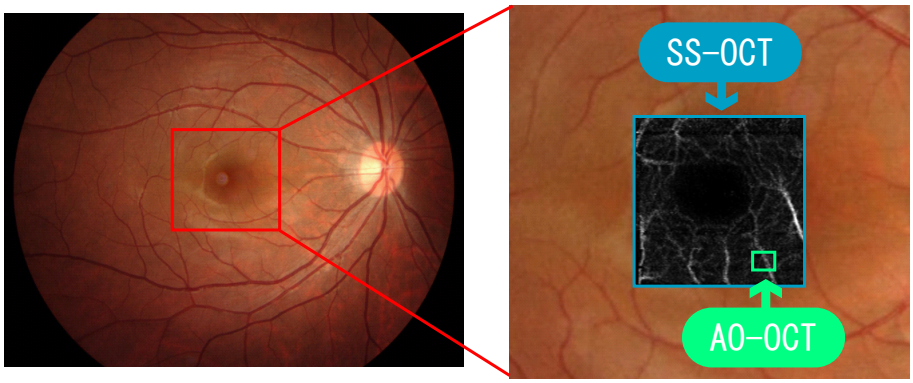

Figure 3.1: Measured area in fundus image. Typical retinal image size of AO-OCT (0.65 degree × 0.65 degree FOV) and SS-OCT (1.5 mm × 1.5 mm) is shown.

Doppler and amplitude decorrelation projections are generated using a single volume. The eccentricity was set to be 5-degree Nasal.

In Section 3.3.2.3, enhanced capillary imaging performance was assessed by examining 4 eyes of 4 healthy subjects. The images are acquired more rapidly than the scanning protocol B to suppress the involuntary motion artifacts. Five sequential volumes were acquired and were used to generate the OCT-based angiographic images: averaged intensity, amplitude decorrelation, and averaged Doppler (Eqs.3.1, 3.2 and 3.3). The eccentricity was set to be 5-degree Nasal.

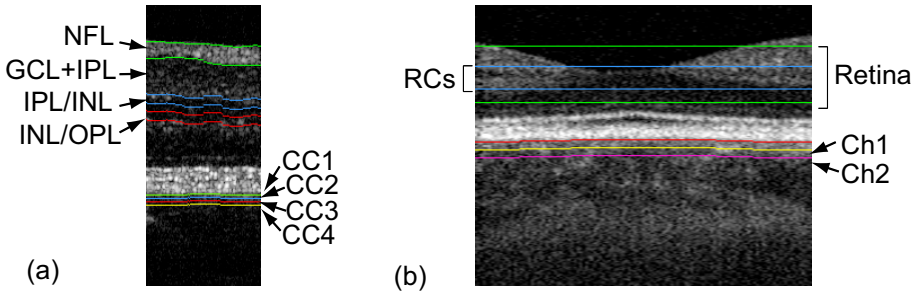

Figure 3.2: Representative B-scan images with segmentation results are shown in (a) by 1-μm AO-OCT and (b) using the SS-OCT. The corresponding depths are indicated by black arrows.

3.3 Results

3.3.1 *In vivo* micro-vascular imaging by SS-OCT

3.3.1.1 Enhanced contrast micro-vascular imaging

In order to image the depth-resolved capillary network, the layer segmentation was performed as shown in Fig. 3.2(b).

Retinal and INL projections of micro-vasculature are shown in Figs. 3.3(a) and (b), respectively. Overall, the scattering information tend to provide better visibility of retinal micro-vasculature.

The choroidal projections of micro-vasculature are shown in Figs. 3.4(b). The choroidal capillary networks in the Sattler's layer are more clearly observed in the averaged Doppler algorithm than the others. Similarly, moderate contrast was observed in the amplitude decorrelation images.

3.3.2 *In vivo* capillary imaging by AO-OCT

3.3.2.1 Depth-resolved capillary network

In order to image the depth-resolved capillary network, the layer segmentation was performed as shown in Fig. 3.2(a).

The retinal capillaries were observed in the averaged intensity and averaged Doppler images as shown in Fig. 3.5(a). In the GCL and IPL projection, a relatively large blood vessel was imaged. No corresponding structure was observed at deeper projections. At the IPL/INL boundary, the retinal capillary bed was more observed in the averaged Doppler image than the corresponding intensity image. At the INL/OPL boundary, the high contrast retinal capillary bed was observed in both the averaged intensity and averaged Doppler images. Here the hyper scatterers, which would mainly be red blood cells, had sufficient contrast to discriminate the capillaries from the static tissue.

On the other hand, in the choroid, the averaged intensity and averaged Doppler images had different contrasts as shown in Fig. 3.5(b). Although the averaged Doppler images

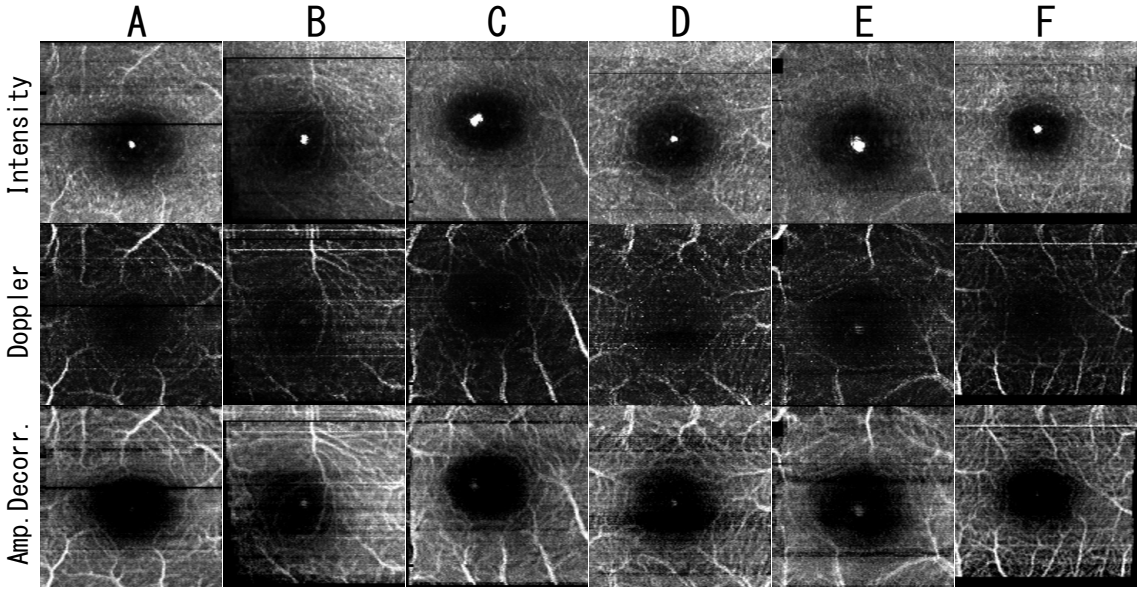

(a)

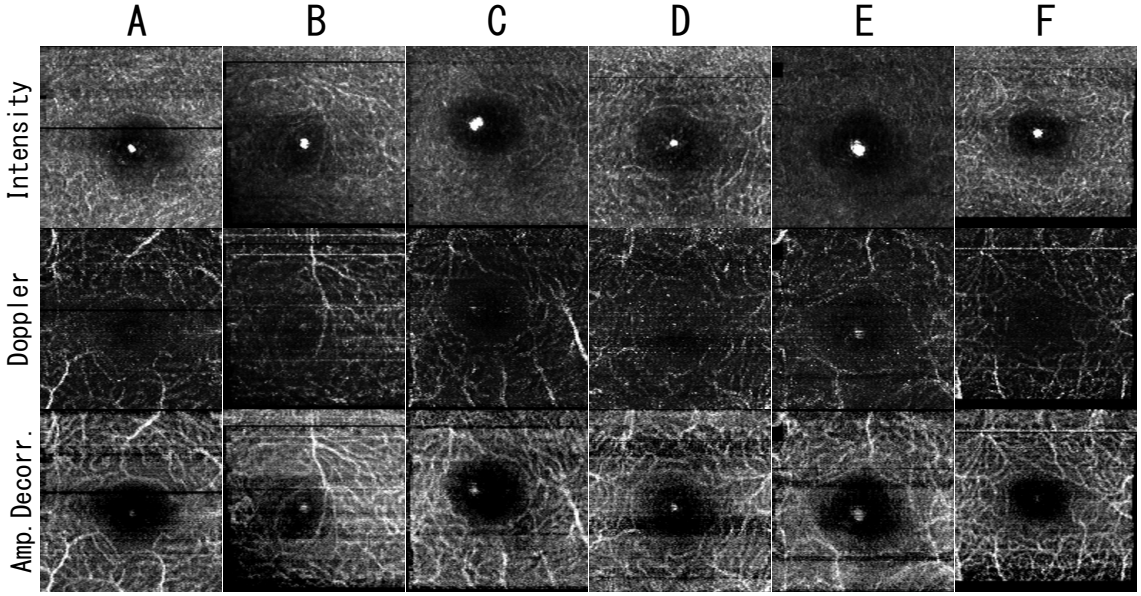

(b)

Figure 3.3: (a)*En face* projections of retinal layer. (b)*En face* projections of INL. The averaged intensity is in linear scale. The retinal image size is 1.5 mm × 1.5 mm.

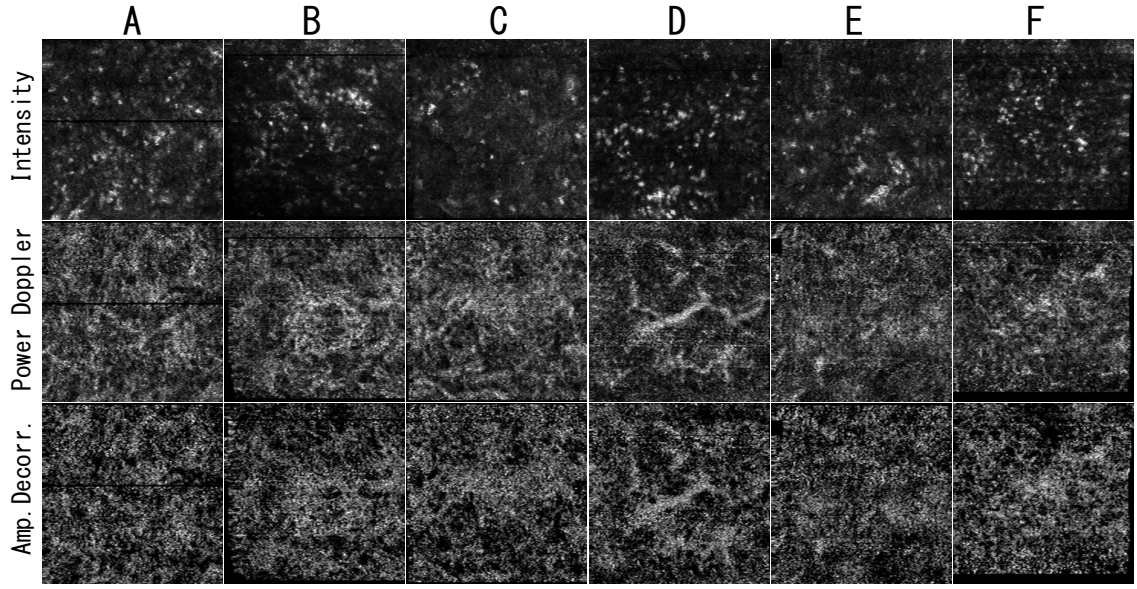

(a)

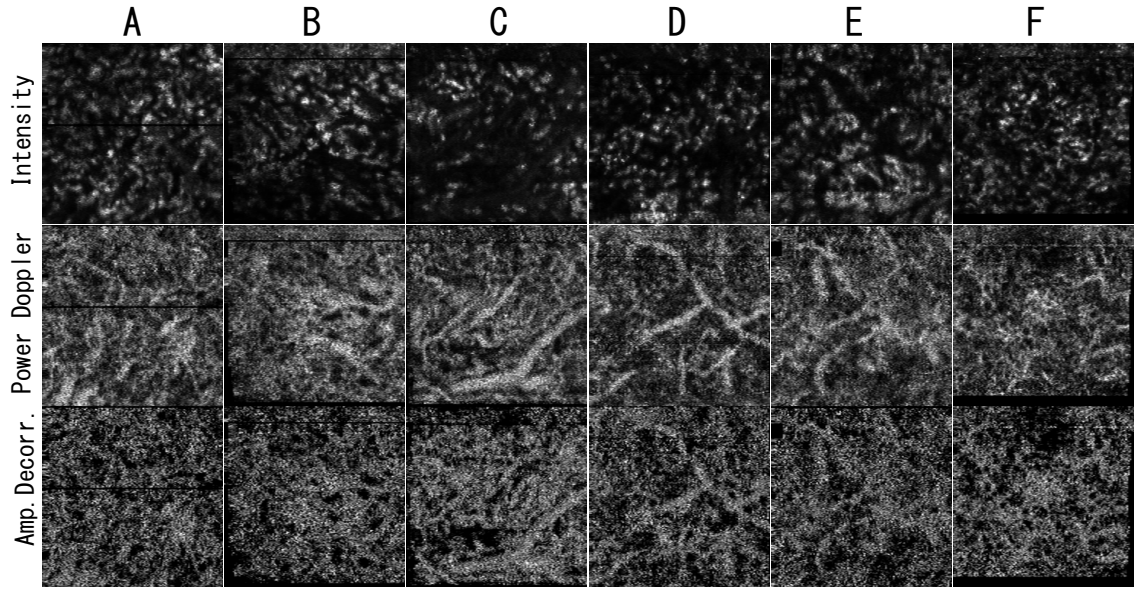

(b)

Figure 3.4: (a)*En face* projections of choroidal micro-vasculature in Sattler's layer. (b)*En face* projections of choroidal micro-vasculature in Sattler's layer. The averaged intensity is in linear scale. The retinal image size is 1.5 mm × 1.5 mm.

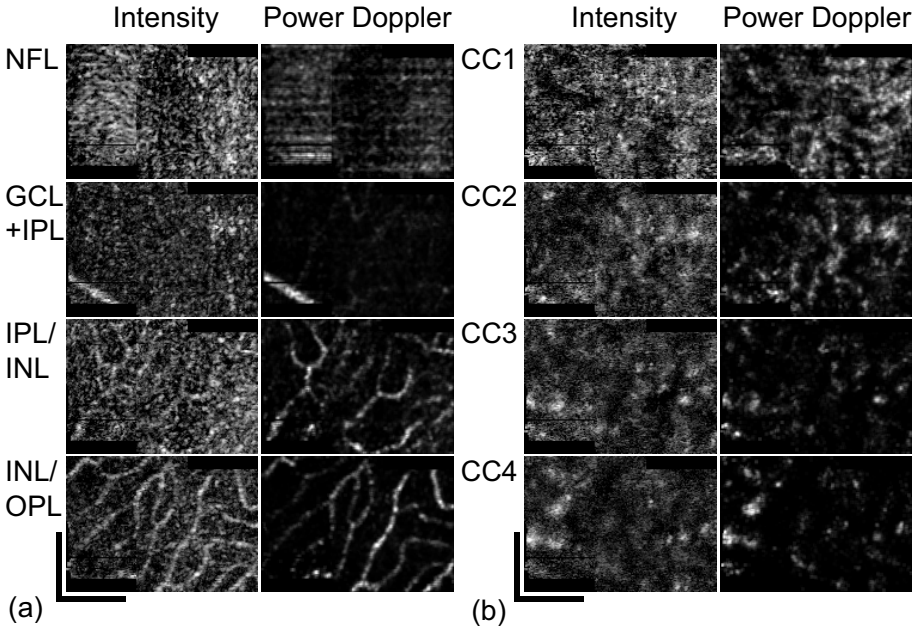

Figure 3.5: (a) *En face* projections of retinal capillaries. (b) *En face* projections of the choriocapillaries layer and choroidal capillary in the Sattler layer. The averaged intensity images are shown in logarithmic scale. A black bar indicates 100 μm.

showed the capillary patterns in projections CC1 and CC2, the corresponding patterns were rarely visible in the averaged intensity images.

3.3.2.2 Choriocapillaris imaging

En face projections of INL/OPL boundary and photoreceptor layer are shown in Figs. 3.6(a) and (b), respectively. The retinal capillaries and cone-photoreceptor cells are visualized, and the results indicate the improvement of lateral resolution. At the same time, *en face* projection of choriocapillaris layer is shown in Figs. 3.6(c)-(e). Obviously, the capillary pattern was rarely visible in the intensity image as shown in Fig. 3.6(c). However, averaged Doppler images show clear capillary pattern as shown in Fig. 3.6(d). Amplitude decorrelation images show moderate capillary pattern, as shown in Fig. 3.6(e). It is clear that choriocapillaris have a more dense capillary network than the retinal capillaries.

3.3.2.3 Enhanced contrast capillary imaging

The retinal capillaries and choriocapillaries are successfully observed for all eyes. The success rates were 83%, 58% 85%, and 78% for subject A, C, D, and E, respectively. Here, the success rate was defined as following exclusion criteria: First, the images should be successfully acquired, in other words, there are no operational errors. Second, the images can be registered each other, in other words, the effect of significant transversal motions (saccade) was not dominant or negligible in the dataset, and the reference image has no

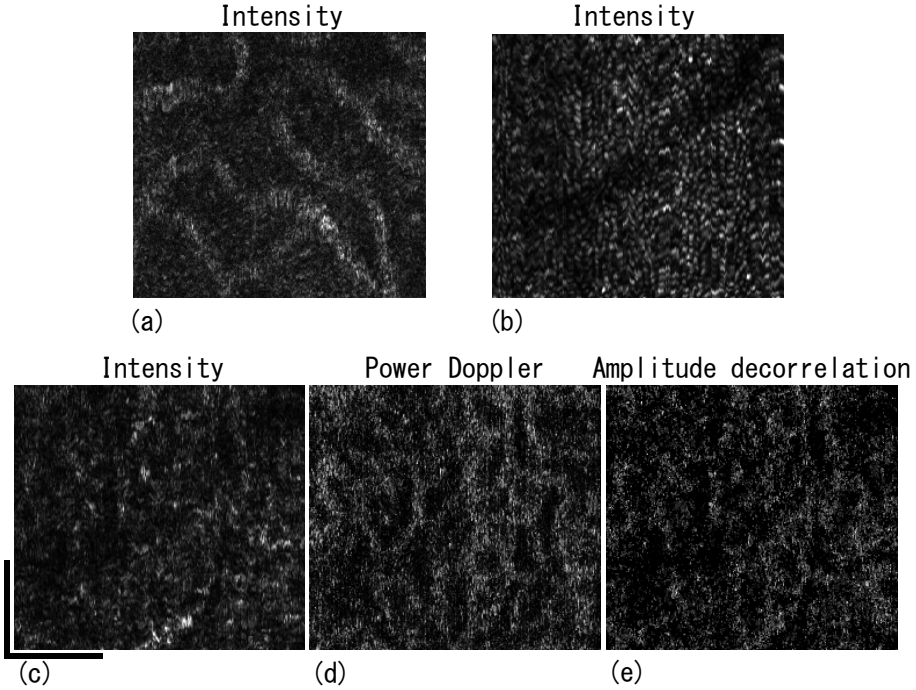

Figure 3.6: (a) *En face* projection of INL/OPL boundary in linear scale. (b) *En face* projection of photoreceptor layer in linear scale. (c)-(e) *En face* projections of the choriocapillaries layer. No moving average filter was applied. A black bar indicates 100 μm.

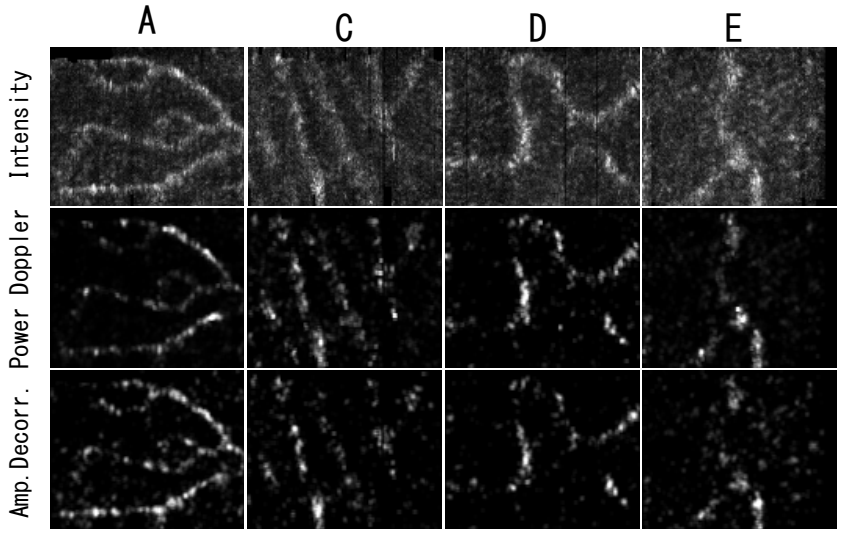

Figure 3.7: *En face* projections of retinal capillaries at the INL/OPL boundary (0.65 degree × 0.65 degree FOV). The averaged intensity is in linear scale.

significant transversal motions.

En face projections at the boundary INL/OPL are shown in Figs. 3.7. In the averaged intensity images, the retinal capillaries were clearly observed. However, average Doppler and amplitude decorrelation images have rather discontinuous patterns.

En face projection of choriocapillaris is shown in Fig. 3.8. The capillary pattern was hardly observed in the intensity images. However, the average Doppler and amplitude decorrelation images show clear capillary pattern. Some amplitude decorrelation images show the signals from inter-capillary regions, although the average Doppler does not.

3.3.3 Selections of threshold level

3.3.4 Contrast stretching

In order to enhance the image contrast, *en face* images are normalized by taking certain percentiles (see Subsection 3.2.1.3). However, the amplitude decorrelation have a larger background than the others. Hence, the lower percentile of the amplitude decorrelation was only different from the others.

The effect of this different lower percentile is shown in Figs. 3.9(a) and (b). It was found that the effect of different lower percentile was more obvious in the choroidal capillary and choriocapillaris images. However, it has a little effect to improve the visibility of the capillary network.

3.3.5 Threshold function in the angiographic algorithms

The important part of the angiographic algorithms is the threshold function T' (see Section 3.2.1.2). Here, the effect of threshold level was examined. For that purpose, we defined

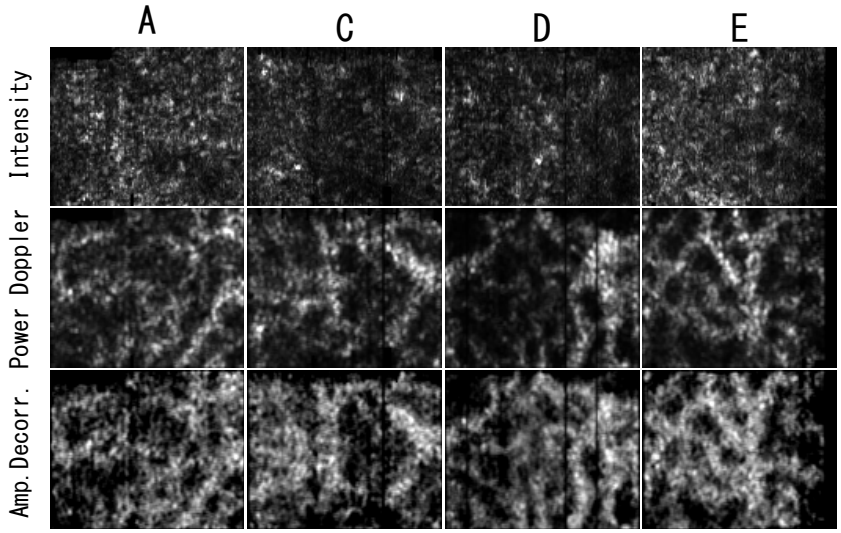

Figure 3.8: *En face* projections of choriocapillaris layer (0.65 degree × 0.65 degree FOV). The averaged intensity is in linear scale.

several threshold functions and calculated the angiographic images.

For the averaged Doppler and amplitude decorrelation, we applied following threshold functions, T'_{6dB}, T'_{8dB}, T'_{10dB} and T'_{12dB}. We rejected the pixels if the magnitude of correlation function from the noise floor $10\log\frac{\sum_{m=1}^{M}|\Gamma_m(\mathbf{r})\Gamma^*_{m+1}(\mathbf{r})|}{M\sigma^2}$ is less than 6, 8, 10 and 12 dB, respectively. On the other hands, for the averaged intensity, we applied simple intensity masks, T''_{6dB}, T''_{8dB}, T''_{10dB} and T''_{12dB}. We rejected the pixels if the SNR $10\log\frac{|\Gamma_m|^2}{\sigma^2}$ of corresponding pixels is less than 6, 8, 10 and 12 dB. In practice, the difference between T' and T'' was negligible.

In addition to the angiographic images, several *en face* images of intensity mask T'' were generated for each threshold level, which is denoted as "Mask" in Figs. 3.10. We selected a single *en face* image of a single volume, which are positioned at the middle of INL/OPL projection and CC1 projection.

Overall, figures 3.10 show that the effect of threshold level was more significant in the averaged Doppler and amplitude decorrelation. The averaged intensity was nearly identical though the different threshold levels were applied.

It should be noted that, in the retina, the intensity mask T''_{12dB} and averaged intensity can discriminate the retinal capillaries as shown in Figs. 3.10(a). However, the higher threshold level suppress the overall signals in the averaged Doppler and amplitude decorrelation. In addition, the vessel images become discontinuous. On the other hands, in the choroid, the choriocapillaris was not discriminated by the intensity mask and averaged intensity. The different threshold levels have a little effect on the averaged Doppler and amplitude decorrelation.

As mentioned in Subsection 3.3.2.3, with the threshold level 6 dB, the artificial signals in the inter-capillary region of retinal capillaries and choriocapillaris were more obvious in the amplitude decorrelation images than the averaged Doppler. The details are discussed

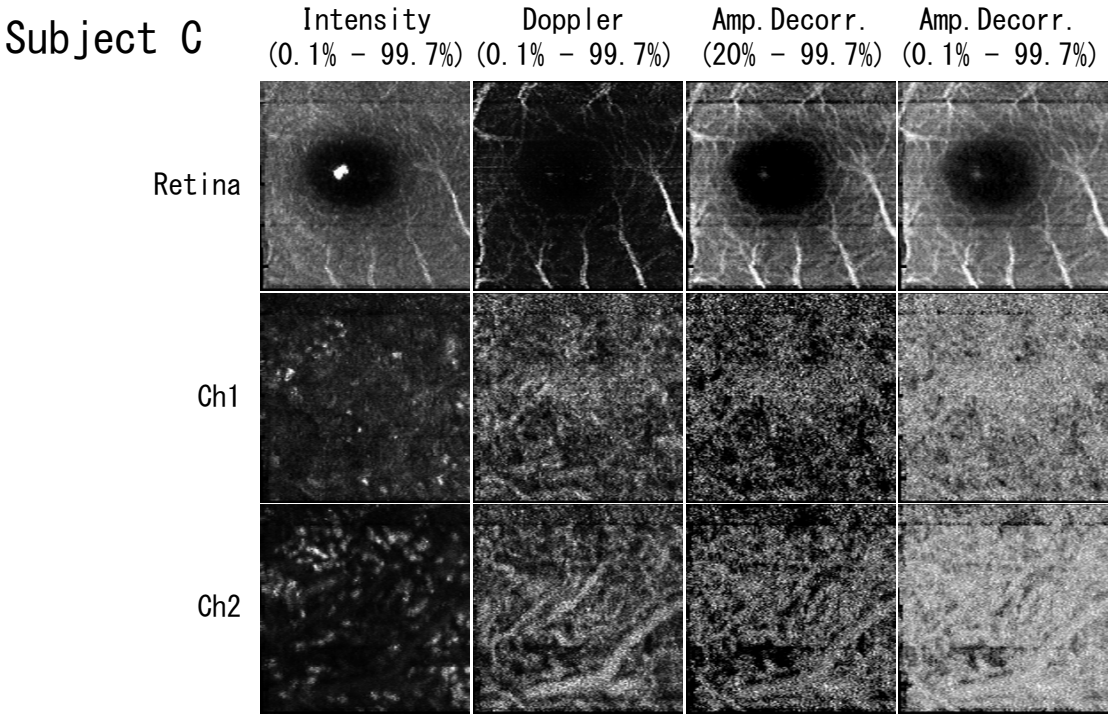

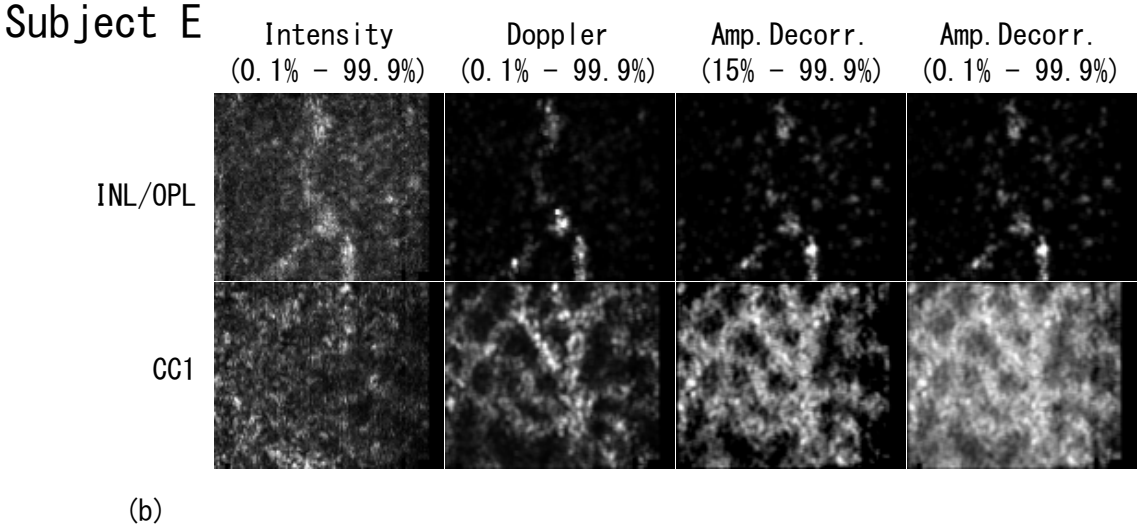

Figure 3.9: (a) *En face* projections of retinal and choroidal layers which is imaged by SS-OCT (1.5 mm × 1.5 mm FOV). The amplitude decorrelation images only are shown in different normalization parameters. (b) *En face* projections of retinal and choroidal layers which is imaged by AO-OCT (0.65 degree × 0.65 degree FOV). The amplitude decorrelation images only are shown in different normalization parameters.

in Subsection 3.4.1.

3.4 Discussion

3.4.1 Equivalence and difference between angiographic algorithms

The correlation function $\langle \Gamma(\mathbf{r},t)\Gamma^*(\mathbf{r},t+\Delta t)\rangle$ is a fundamental quantity to represent the temporal variance of interferometric signals. For instance, the attenuation of the correlation function represents the temporal changes of complex OCT signals [47, 48]. Furthermore, if we focused on the amplitude variance of the correlation function $\langle |\Gamma(\mathbf{r},t)||\Gamma^*(\mathbf{r},t+\Delta t)|\rangle$, it is equivalent to measure time-varying speckles [28,29]. On the other hands, if we focused on the phase-shift of correlation function $Arg\big(\langle \Gamma(\mathbf{r},t)\Gamma^*(\mathbf{r},t+\Delta t)\rangle\big)$, it is equivalent to measure Doppler frequency shift [42–45]. Thus, it is known that the approaches between time-varying speckle and Doppler measurement are nearly identical in the measurement of line-of-sight velocity [40].

However, this equivalence is true if the moving sample is a mirror or homogeneous scattering sample. In practice, the sample have a heterogeneous structure, the effective number of scatterers and spatially varying speckles also contributes the speckle contrast [115]. In addition, the other intensity fluctuation cause the speckle variance. They make a difference between the algorithms.

For example, the amplitude decorrelation is known to be useful to detect in-plane flow velocity. However, it is also affected by other amplitude fluctuations: incident beam power, incident beam angles, spatially-varying speckles and effective number of scatterers which contributes the interferences. It might result in the background signals in the inter-capillary region (see Subsections 3.3.2.3 and 3.3.5) and moderate image qualities (see Subsections 3.3.1.1 and 3.3.2.2).

On the other hand, the Doppler OCT measures the subtle sub-pixel axial displacement. Although the phase wrappings occurred, the detection of Doppler shift is nearly identical to that of time-varying speckles. The important point is that the intensity variation does not alter the Doppler shift though phase noise is dependent on the SNR. Since the intensity threshold is applied, the more reliable signals are extracted from multiple-volumes. This maneuver allows to suppress the phase noise.

Amplitude decorrelation Amplitude decorrelation is derived from a correlation function of amplitude of OCT signals. And hence, it is essentially equivalent to measure the time-varying amplitude of the sample. In fact, the amplitude decorrelation is equivalent to the amplitude differentiation as

$$\begin{aligned}\Delta|\Gamma| &= \sum_{i}^{N}\left(1-\frac{2|\Gamma_i||\Gamma_{i+1}|}{I_i+I_{i+1}}\right)\\ &= \sum_{i}^{N}\frac{(|\Gamma_i|-|\Gamma_{i+1}|)^2}{I_i+I_{i+1}},\end{aligned} \tag{3.5}$$

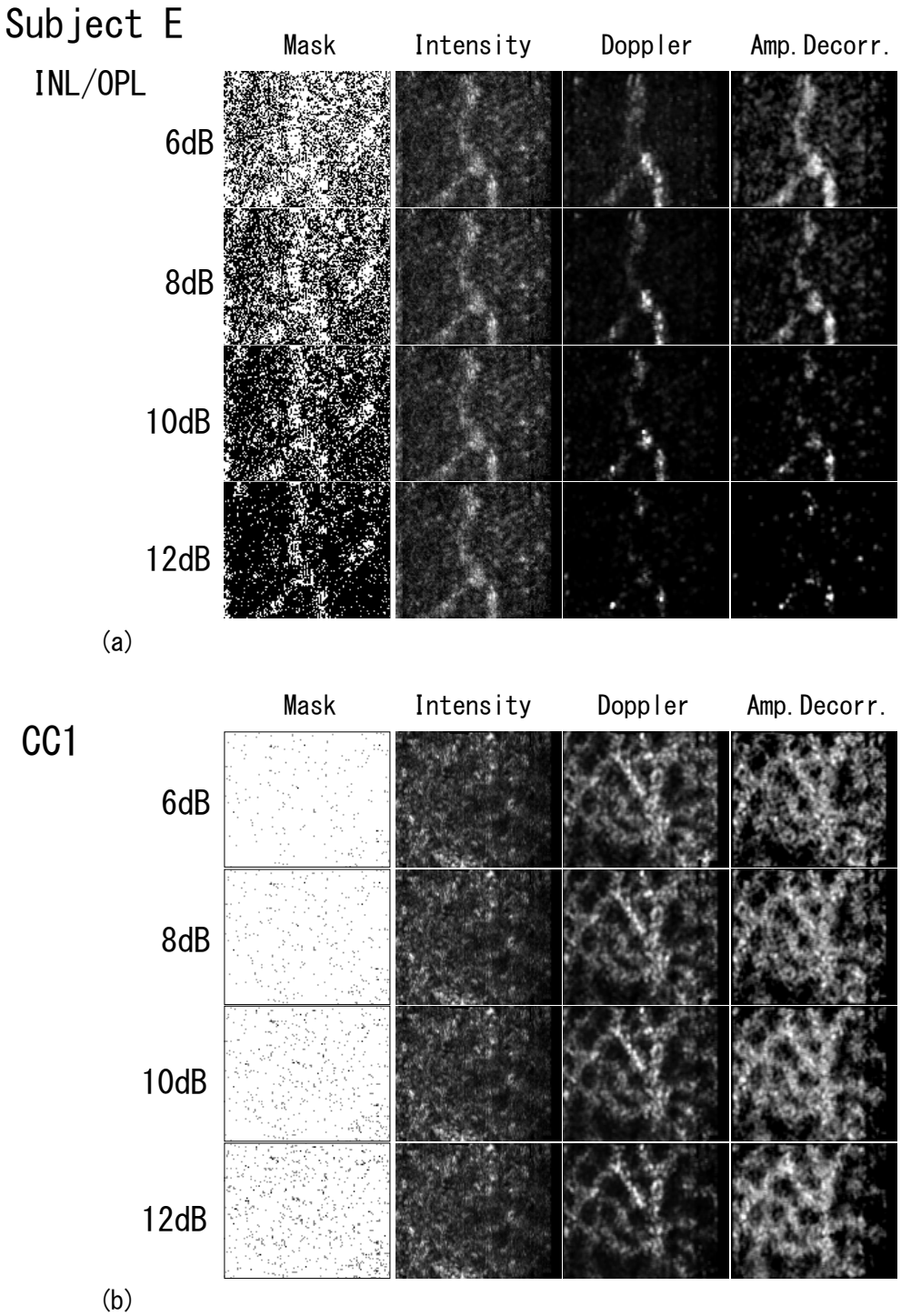

Figure 3.10: *En face* images of INL/OPL projection (a) and CC1 projection (b), which is imaged by 1-μm AO-OCT (0.65 degree $\times$ 0.65 degree FOV). The intensity mask, averaged intensity, averaged Doppler and amplitude decorrelation images are generated.

Averaged Doppler It should be noted that the averaged power of Doppler phase-shift is essentially equivalent to the phase-shift variance with the large number of samples. Here, the phase-shift variance is described as [26, 27]

$$\sigma^2_{\Delta\phi}(z) = \frac{1}{N}\sum_i^N \left(\Delta\phi(z) - \frac{1}{N}\sum_i^N \Delta\phi(z)\right)^2, \tag{3.6}$$

If N is sufficiently large, the mean of phase-shift approaches to zero, since the capillary velocity and phase noise are random. Hence, the averaged Doppler phase-shift is now described as

$$\lim_{n\to\infty} \frac{1}{N}\sum_i^N \Delta\phi(z) \approx 0, \tag{3.7}$$

and hence,

$$\sigma^2_{\Delta\phi}(z) \approx \frac{1}{N}\sum_i^N \left(\Delta\phi(z)\right)^2, \tag{3.8}$$

Thus, the mean subtraction does not significantly change the results. The averaged power is more simple and computationally inexpensive.

3.4.2 Choriocapillaris

Although choriocapillaris imaging has been reported using FA [116] and ICGA [117], neither of the methods provide the microscopic structure of the choriocapillaris. In addition, the limited depth resolution of FA and ICGA prohibits the three-dimensional investigation of the choroidal capillary network. Furthermore FA and ICGA are not noninvasive methods and induce some adverse reactions. The issues of the limited transversal and depth resolutions can be overcome by AO-OCT. Torti et al. demonstrated choriocapillaris imaging by AO-OCT [71]. However, the imaging was only performed with intensity OCT and not with Doppler OCT. In our result, intensity OCT showed only limited contrast, and the choriocapillaris were rarely visible. Alternatively, the averaged Doppler and amplitude decorrelation images showed capillary patterns more clearly. Especially, averaged Doppler, which is derived from phase-information of OCT, was found to be more suitable for the choroidal micro-vasculature imaging.

The reasons of the limited contrast in the intensity images can be explained by the scattering properties of tissues. According to the histology, the inter-capillary region contains collagen fibers [118]. Except the special case of cornea, collagenous tissue, such as sclera and lamina cribrosa, appeared with hyper-scattering in the OCT intensity image. Since the capillary is also hyper-scattering, this scattering property of the inter-capillary region would degrade the contrast of the choriocapillaris in the intensity images.

3.4.3 Limitations

The current study has several limitations. The most severe limitation is again that of involuntary eye motion. For high-sensitivity Doppler imaging, a highly dense scanning protocol (i.e., a protocol with a smaller fractional displacement) is required. Since the higher density of scanning requires a longer measurement time, the imaging is more easily disturbed by involuntary eye motion. However, this problem would be overcome by high-speed OCT imaging technology [81, 82].

The imperfection of image registration causes the larger variance and results in artifacts. The more accurate image registration algorithm will allow more stable results and reduce the total datasets and calculation time.

The capillary images are observed qualitatively and not quantitatively. The capillary segmentation algorithm is required for the quantification. The robust and fast algorithm are essential for the volumetric quantification.

3.5 Summary

In summary, we successfully enhance the vasculature image contrast using several multiple-volume OCT-based angiographic algorithms. The results of the SS-OCT showed high-contrast retinal micro-vascular images for all eyes. The slight change of vascular contrast was found between the angiographic algorithms. However, in the case of the choroid, the choroidal capillary networks in the Sattler's layer were more clearly observed in the averaged Doppler image than the others.

The similar tendency was observed in the images taken by AO-OCT. The choriocapillaris was more visualized by averaged Doppler shift and amplitude decorrelation. The choriocapillaris were rarely visible in the averaged intensity image.

In conclusion, Doppler technique was found to be useful especially for the detection of choriocapillaris and choroidal capillary network in the Sattler's layer.

Chapter 4

Conclusion

In conclusion, we successfully enhances the capillary imaging performance of ophthalmic OCT by developing 1-μm AO-OCT and using several multiple-volume OCT angiographic algorithms. To the best of our knowledge, we are the first to demonstrate the AO-OCT combining with the OCT-based angiographic methods. This enables the detailed investigation of a three-dimensional capillary network in the retina and choroid.

In vivo photoreceptor cells were resolved at 4–5 degree Nasal by 1-μm AO-OCT, which were rarely observed without AO. Although the involuntary motion artifacts were significant, the lateral resolution and OCT signals were improved with AO.

Multiple-volume OCT angiographic algorithms further enhance the vasculature image contrast. The retinal capillaries have been successfully imaged by averaged intensity, amplitude decorrelation, and averaged power of Doppler shift. The choriocapillaris and choroidal capillary network in the Sattler's layer were more highly contrasted by the Doppler technique than the others. It was found that the combination of Doppler techniques and AO-and SS-OCT is especially useful for the detection of choriocapillaris and choroidal capillary network. In addition, the combination of the SS-OCT and 1-μm AO-OCT is capable of a more comprehensive vascular imaging in addition to the structural imaging.

Appendix

Limitation of wavefront modulation

The achievable smallest residual wavefront error increases by introducing a target slope. The residual wavefront error, or so-called a target reconstruction error, increases roughly in proportion to the difference of the shapes of deformable mirror at the initial state and the state which perfectly generates the target wavefront. This theoretical limit on the target reconstruction error is discussed in this Appendix. The theoretical limit is important because the practically applicable amount of SA of our method was limited by this factor.

Assume AO closed loop is driven by an integral controller. The measured slope vector at n-th iteration of the AO closed loop $\mathbf{s}_e$ will be given by

$$\mathbf{s}_e(t_n) = \mathbf{s}_f - \mathbf{s}_v(t_{n-1}) \tag{4.1}$$

where t is time, n is the number of iterations of the AO closed loop, $\mathbf{s}_f$ is a constant slope vector which represents the static total aberration of the system and the aberration of a sample when the deformable mirror is flattened, and $\mathbf{s}_v$ is a reconstructed slope vector which is defined as

$$\mathbf{s}_v(t_n) = \mathbf{A}\mathbf{v}(t_{n-1}) - \alpha\mathbf{A}\mathbf{A}^{+}(\mathbf{s}_e(t_n) - \mathbf{s}_{target}) \tag{4.2}$$

where $\mathbf{A}$ is an influence matrix of the AO-setup, $\mathbf{A}^*$ is the Moore-Penrose pseudo inverse matrix of $\mathbf{A}$, and α represents a closed-loop gain. $\mathbf{s}_{target}$ is a target slope vector.

As described in Section 1.3, a command vector at the time of t_n with the target slope vector is defined as

$$\mathbf{v}(t_n) = \mathbf{v}(t_{n-1}) - \alpha\mathbf{A}^{+}(\mathbf{s}_e(t_n) - \mathbf{s}_{target}) \tag{4.3}$$

From Eqs. (4.1)-(4.3), the expected slope vector can be rewritten as

$$\mathbf{s}_e(t_n) = \mathbf{s}_f - \alpha\mathbf{A}\mathbf{A}^{+}\sum_{i=0}^{n-1}(\mathbf{s}_e(t_i) - \mathbf{s}_{target}) \tag{4.4}$$

Here, the expected slope vector after subtraction of the target slope vector is defined as

residual error $\mathbf{s}'_e(t_n)$

$$\begin{aligned}\mathbf{s}'_e(t_n) &\equiv \mathbf{s}_e(t_n) - \mathbf{s}_{target} \\ &= \mathbf{s}_f - \alpha\mathbf{A}\mathbf{A}^+ \sum_{i=0}^{n-1}(\mathbf{s}_e(t_i) - \mathbf{s}_{target}) - \mathbf{s}_{target} \\ &= (\mathbf{I} - \alpha\mathbf{A}\mathbf{A}^+)^n\mathbf{s}_f - (\mathbf{I} - \alpha\mathbf{A}\mathbf{A}^+)^{n-1}\mathbf{s}_{target} \end{aligned} \tag{4.5}$$

In Eq. (4.5), if n is sufficiently large and the sample is static, residual error $\mathbf{s}'_e(t_n)$ can expressed as

$$\begin{aligned}\mathbf{s}''_e(t_n) &\equiv \lim_{n\to\infty} \mathbf{s}'_e(t_n) \\ &= (\mathbf{I} - \mathbf{A}\mathbf{A}^+)(\mathbf{s}_f - \mathbf{s}_{target}) \end{aligned} \tag{4.6}$$

where the following relation was used

$$\begin{aligned}\lim_{n\to\infty}(\mathbf{I} - \alpha\mathbf{A}\mathbf{A}^+)^n &= \lim_{n\to\infty}(\mathbf{I} - \mathbf{A}\mathbf{A}^+ + (1-\alpha)^n\mathbf{A}\mathbf{A}^+) \\ &= \mathbf{I} - \mathbf{A}\mathbf{A}^+ \end{aligned} \tag{4.7}$$

Equation 4.6 indicates that if $\mathbf{A}\mathbf{A}^+$ is unity, the target reconstruction error is always zero. However, in practice, $\mathbf{A}\mathbf{A}^+ \neq \mathbf{I}$. Under this practical condition, residual aberration becomes larger as the change of the deformable mirror from its initial state is larger.

This means when we start the closed loop with a flattened deformable mirror, a larger target slope raises a larger minimally achievable residual error.

Note that this discussion is based on an assumption that the sample has a constant aberration in time. If the sample has a dynamic aberration, this effect becomes more severe, which can be modeled by converting $\mathbf{s}_f$ to $\mathbf{s}_f(t_n)$ in the Eq. (4.1), although $\mathbf{s}_f(t_n)$ is not predictable.

Bibliography

[1] D. Huang, E. A. Swanson, C. P. Lin, J. S. Schuman, W. G. Stinson, W. Chang, M. R. Hee, T. Flotte, K. Gregory, C. A. Puliafito, and a. et, "Optical coherence tomography," Science **254**, 1178–1181 (1991).

[2] G. Häusler and M. W. Lindner, ""coherence radar" and "spectral radar" tools for dermatological diagnosis," Journal of Biomedical Optics **3**, 21–31 (1998).

[3] T. Mitsui, "Dynamic range of optical reflectometry with spectral interferometry," Japanese Journal of Applied Physics **38**, 6133–6137 (1999).

[4] R. Leitgeb, C. Hitzenberger, and A. Fercher, "Performance of fourier domain vs. time domain optical coherence tomography," Optics Express **11**, 889–894 (2003).

[5] J. F. de Boer, B. Cense, B. H. Park, M. C. Pierce, G. J. Tearney, and B. E. Bouma, "Improved signal-to-noise ratio in spectral-domain compared with time-domain optical coherence tomography," Optics Letters **28**, 2067–2069 (2003).

[6] W. Drexler and J. G. Fujimoto, "State-of-the-art retinal optical coherence tomography," Progress in Retinal and Eye Research **27**, 45 – 88 (2008).

[7] A. Alm, "Circulation," in "Adler's Physiology of the Eye," , P. L. Kaufman and A. Alm, eds. (Mosby, 2002), pp. 747–784, 10th ed.

[8] A. Iwase, M. Araie, A. Tomidokoro, T. Yamamoto, H. Shimizu, and Y. Kitazawa, "Prevalence and causes of low vision and blindness in a japanese adult population: The tajimi study," Ophthalmology **113**, 1354–1362.e1 (2006).

[9] D. Pascolini and S. P. Mariotti, "Global estimates of visual impairment: 2010," British Journal of Ophthalmology (2011).

[10] J. Liang, D. R. Williams, and D. T. Miller, "Supernormal vision and high-resolution retinal imaging through adaptive optics," J. Opt. Soc. Am. A **14**, 2884–2892 (1997).

[11] B. Hermann, E. J. Fernández, A. Unterhuber, H. Sattmann, A. F. Fercher, W. Drexler, P. M. Prieto, and P. Artal, "Adaptive-optics ultrahigh-resolution optical coherencetomography," Optics Letters **29**, 2142–2144 (2004).

[12] Y. Zhang, J. Rha, R. Jonnal, and D. Miller, "Adaptive optics parallel spectral domain optical coherence tomography for imaging the living retina," Opt. Express **13**, 4792–4811 (2005).

[13] R. Zawadzki, S. Jones, S. Olivier, M. Zhao, B. Bower, J. Izatt, S. Choi, S. Laut, and J. Werner, "Adaptive-optics optical coherence tomography for high-resolution and high-speed 3D retinal in vivo imaging," Optics Express **13**, 8532–8546 (2005).

[14] E. J. Fernández, B. Považay, B. Hermann, A. Unterhuber, H. Sattmann, P. M. Prieto, R. Leitgeb, P. Ahnelt, P. Artal, and W. Drexler, "Three-dimensional adaptive optics ultrahigh-resolution optical coherence tomography using a liquid crystal spatial light modulator," Vision Research **45**, 3432–3444 (2005).

[15] Y. Yasuno, Y. Hong, S. Makita, M. Yamanari, M. Akiba, M. Miura, and T. Yatagai, "In vivo high-contrast imaging of deep posterior eye by 1-um swept source optical coherence tomography andscattering optical coherence angiography," Opt. Express **15**, 61216139 (2007).

[16] T. Schmoll, A. S. G. Singh, C. Blatter, S. Schriefl, C. Ahlers, U. Schmidt-Erfurth, and R. A. Leitgeb, "Imaging of the parafoveal capillary network and its integrity analysis using fractal dimension," Biomed. Opt. Express **2**, 11591168 (2011).

[17] R. Motaghiannezam, D. Schwartz, and S. E. Fraser, "In vivo human choroidal vascular pattern visualization using high speed swept source optical coherence tomography at 1060 nm," Investigative Ophthalmology & Visual Science (2012).

[18] R. Motaghiannezam and S. Fraser, "Logarithmic intensity and speckle-based motion contrast methods for human retinal vasculature visualization using swept source optical coherence tomography," Biomedical Optics Express **3**, 503–521 (2012).

[19] C. Blatter, T. Klein, B. Grajciar, T. Schmoll, W. Wieser, R. Andre, R. Huber, and R. A. Leitgeb, "Ultrahigh-speed non-invasive widefield angiography," Journal of Biomedical Optics **17**, 070505–070505–3 (2012).

[20] I. Grulkowski, I. Gorczynska, M. Szkulmowski, D. Szlag, A. Szkulmowska, R. A. Leitgeb, A. Kowalczyk, and M. Wojtkowski, "Scanning protocols dedicated to smart velocity ranging in spectral OCT," Optics Express **17**, 23736–23754 (2009).

[21] L. An, T. T. Shen, and R. K. Wang, "Using ultrahigh sensitive optical microangiography to achieve comprehensive depth resolved microvasculature mapping for human retina," Journal of Biomedical Optics **16**, 106013–106013–9 (2011).

[22] Y.-J. Hong, S. Makita, F. Jaillon, M. J. Ju, E. J. Min, B. H. Lee, M. Itoh, M. Miura, and Y. Yasuno, "High-penetration swept source doppler optical coherence angiography by fully numerical phase stabilization," Optics Express **20**, 2740–2760 (2012).

[23] B. Braaf, K. V. Vienola, C. K. Sheehy, Q. Yang, K. A. Vermeer, P. Tiruveedhula, D. W. Arathorn, A. Roorda, and J. F. de Boer, "Real-time eye motion correction in

phase-resolved OCT angiography with tracking SLO," Biomedical Optics Express **4**, 51–65 (2013).

[24] S. Makita, F. Jaillon, M. Yamanari, and Y. Yasuno, "Dual-beam-scan doppler optical coherence angiography for birefringence-artifact-free vasculature imaging," Optics Express **20**, 2681–2692 (2012).

[25] S. Zotter, M. Pircher, T. Torzicky, M. Bonesi, E. Gtzinger, R. A. Leitgeb, and C. K. Hitzenberger, "Visualization of microvasculature by dual-beam phase-resolved doppler optical coherence tomography," Optics Express **19**, 1217–1227 (2011).

[26] J. Fingler, R. J. Zawadzki, J. S. Werner, D. Schwartz, and S. E. Fraser, "Volumetric microvascular imaging of human retina using optical coherence tomography with a novel motion contrast technique," Optics Express **17**, 22190–22200 (2009).

[27] D. Y. Kim, J. Fingler, J. S. Werner, D. M. Schwartz, S. E. Fraser, and R. J. Zawadzki, "In vivo volumetric imaging of human retinal circulation with phase-variance optical coherence tomography," Biomedical Optics Express **2**, 1504–1513 (2011).

[28] G. Liu, L. Chou, W. Jia, W. Qi, B. Choi, and Z. Chen, "Intensity-based modified doppler variance algorithm: application to phase instable and phase stable optical coherence tomography systems," Optics Express **19**, 11429–11440 (2011).

[29] Y. Jia, O. Tan, J. Tokayer, B. Potsaid, Y. Wang, J. J. Liu, M. F. Kraus, H. Subhash, J. G. Fujimoto, J. Hornegger, and D. Huang, "Split-spectrum amplitude-decorrelation angiography with optical coherence tomography," Optics Express **20**, 4710–4725 (2012).

[30] E. C. Lee, J. F. de Boer, M. Mujat, H. Lim, and S. H. Yun, "In vivo optical frequency domain imaging of human retina and choroid," Optics Express **14**, 4403–4411 (2006).

[31] A. Unterhuber, B. Považay, B. Hermann, H. Sattmann, A. Chavez-Pirson, and W. Drexler, "In vivo retinal optical coherence tomography at 1040 nm - enhanced penetration into the choroid," Opt. Express **13**, 32523258 (2005).

[32] B. Považay, B. Hermann, A. Unterhuber, B. Hofer, H. Sattmann, F. Zeiler, J. E. Morgan, C. Falkner-Radler, C. Glittenberg, S. Blinder, and W. Drexler, "Three-dimensional optical coherence tomography at 1050nm versus 800nm in retinal pathologies: enhanced performance and choroidal penetration in cataract patients," Journal of Biomedical Optics **12**, 041211–041211 (2007).

[33] Y. Chen, D. L. Burnes, M. de Bruin, M. Mujat, and J. F. de Boer, "Three-dimensional pointwise comparison of human retinal optical property at 845 and 1060nm using optical frequency domain imaging," Journal of Biomedical Optics **14**, 024016–024016 (2009).

[34] M. Hammer, A. Roggan, D. Schweitzer, and G. Muller, "Optical properties of ocular fundus tissues-an in vitro study using the double-integrating-sphere technique

and inverse monte carlo simulation," Physics in Medicine and Biology **40**, 963–978 (1995).

[35] W. Drexler and J. G. Fujimoto, eds., *Optical Coherence Tomography: Technology and Applications* (Springer, 2008). ISBN: 978-3-540-77549-2.

[36] A. F. Fercher, C. K. Hitzenberger, G. Kamp, and S. Y. El-Zaiat, "Measurement of intraocular distances by backscattering spectral interferometry," Optics Communications **117**, 43 – 48 (1995).

[37] J. Barton and S. Stromski, "Flow measurement without phase information in optical coherence tomography images," Optics Express **13**, 5234–5239 (2005).

[38] A. Mariampillai, B. A. Standish, E. H. Moriyama, M. Khurana, N. R. Munce, M. K. K. Leung, J. Jiang, A. Cable, B. C. Wilson, I. A. Vitkin, and V. X. D. Yang, "Speckle variance detection of microvasculature using swept-source optical coherence tomography," Opt. Lett. **33**, 15301532 (2008).

[39] J. Ohtsubo and T. Asakura, "Velocity measurement of a diffuse object by using time-varying speckles," Optical and Quantum Electronics **8**, 523–529 (1976).

[40] J. D. Briers, "Laser doppler and time-varying speckle: a reconciliation," Journal of the Optical Society of America A **13**, 345–350 (1996).

[41] J. Walther, A. Krüger, M. Cuevas, and E. Koch, "Effects of axial, transverse, and oblique sample motion in fd oct in systems with global or rolling shutter line detector," Journal of the Optical Society of America A **25**, 2791–2802 (2008).

[42] X. J. Wang, T. E. Milner, and J. S. Nelson, "Characterization of fluid flow velocity by optical doppler tomography," Optics Letters **20**, 1337–1339 (1995).

[43] S. Yazdanfar, A. M. Rollins, and J. A. Izatt, "Imaging and velocimetry of the human retinal circulation with color doppler optical coherence tomography," Opt. Lett. **25**, 14481450 (2000).

[44] R. Leitgeb, L. Schmetterer, W. Drexler, A. Fercher, R. Zawadzki, and T. Bajraszewski, "Real-time assessment of retinal blood flow with ultrafast acquisition by color doppler fourier domain optical coherence tomography," Opt. Express **11**, 31163121 (2003).

[45] B. White, M. Pierce, N. Nassif, B. Cense, B. Park, G. Tearney, B. Bouma, T. Chen, and J. de Boer, "In vivo dynamic human retinal blood flow imaging using ultra-high-speed spectral domain optical coherence tomography," Optics Express **11**, 3490–3497 (2003).

[46] Y. Zhao, Z. Chen, C. Saxer, S. Xiang, J. F. de Boer, and J. S. Nelson, "Phase-resolved optical coherence tomography and optical doppler tomography for imaging blood flow in human skin with fast scanning speed and high velocity sensitivity," Optics Letters **25**, 114–116 (2000).

[47] Y. Zhao, Z. Chen, C. Saxer, Q. Shen, S. Xiang, J. F. d. Boer, and J. S. Nelson, "Doppler standard deviation imaging for clinical monitoring of in vivo human skin blood flow," Opt. Lett. **25**, 13581360 (2000).

[48] L. Wang, Y. Wang, S. Guo, J. Zhang, M. Bachman, G. Li, and Z. Chen, "Frequency domain phase-resolved optical doppler and doppler variance tomography," Optics Communications **242**, 345 – 350 (2004).

[49] J. Porter, H. Queener, J. Lin, K. Thorn, and A. A. S. Awwal, *Adaptive Optics for Vision Science: Principles, Practices, Design and Applications* (Wiley-Interscience, 2006), 1st ed.

[50] D. M. Alloin and J.-M. Mariotti, eds., *Adaptive Optics for Astronomy (Nato Science Series C:* (Springer, 2010), softcover reprint of hardcover 1st ed. 1994 ed.

[51] T. Shirai and C. Dainty, "Adaptive optics as a spatial coherence modifier," Optical Review **11**, 1–3 (2004).

[52] G. Yoon, "Wavefront sensing and diagnostic uses," in "Adaptive Optics for Vision Science," , J. Porter, H. Queener, J. Lin, K. Thorn, and A. A. S. Awwal, eds. (Wiley-Interscience, 2006), pp. 63 – 81, 1st ed.

[53] L. Chen, "Control algorithms," in "Adaptive Optics for Vision Science," , J. Porter, H. Queener, J. Lin, K. Thorn, and A. A. S. Awwal, eds. (Wiley-Interscience, 2006), pp. 119–137, 1st ed.

[54] P. Godara, A. M. Dubis, A. Roorda, J. L. Duncan, and J. Carroll, "Adaptive optics retinal imaging: emerging clinical applications." Optom Vis Sci **87**, 930941 (2010).

[55] A. Roorda, "Adaptive optics for studying visual function: A comprehensive review," J. Vision **11** (2011).

[56] D. T. Miller, O. P. Kocaoglu, Q. Wang, and S. Lee, "Adaptive optics and the eye (super resolution OCT)," Eye **25**, 321–330 (2011).

[57] E. A. Rossi, M. Chung, A. Dubra, J. J. Hunter, W. H. Merigan, and D. R. Williams, "Imaging retinal mosaics in the living eye," Eye **25**, 301308 (2011).

[58] D. R. Williams, "Imaging single cells in the living retina," Vision Research **51**, 1379–1396 (2011).

[59] A. Roorda, F. Romero-Borja, I. Donnelly, H. Queener, T. Hebert, and M. Campbell, "Adaptive optics scanning laser ophthalmoscopy," Optics Express **10**, 405–412 (2002).

[60] S. A. Burns, R. Tumbar, A. E. Elsner, D. Ferguson, and D. X. Hammer, "Large-field-of-view, modular, stabilized, adaptive-optics-based scanning laser ophthalmoscope," J. Opt. Soc. Am. A **24**, 13131326 (2007).

[61] T. Y. Chui, H. Song, and S. A. Burns, "Adaptive-optics imaging of human cone photoreceptor distribution," Journal of the Optical Society of America A **25**, 3021–3029 (2008).

[62] A. Dubra, Y. Sulai, J. L. Norris, R. F. Cooper, A. M. Dubis, D. R. Williams, and J. Carroll, "Noninvasive imaging of the human rod photoreceptor mosaic using a confocal adaptive optics scanning ophthalmoscope," Biomed. Opt. Express **2**, 18641876 (2011).

[63] J. A. Martin and A. Roorda, "Direct and noninvasive assessment of parafoveal capillary leukocyte velocity," Ophthalmology **112**, 2219–2224 (2005).

[64] Z. Zhong, B. L. Petrig, X. Qi, and S. A. Burns, "In vivo measurement of erythrocyte velocity and retinal blood flow using adaptive optics scanning laser ophthalmoscopy," Opt. Express **16**, 1274612756 (2008).

[65] J. Tam, J. A. Martin, and A. Roorda, "Noninvasive visualization and analysis of parafoveal capillaries in humans," Investigative Ophthalmology & Visual Science **51**, 1691–1698 (2010).

[66] J. Tam and A. Roorda, "Speed quantification and tracking of moving objects in adaptive optics scanning laser ophthalmoscopy." J Biomed Opt **16**, 036002 (2011).

[67] J. Tam, P. Tiruveedhula, and A. Roorda, "Characterization of single-file flow through human retinal parafoveal capillaries using an adaptive optics scanning laser ophthalmoscope," Biomed. Opt. Express **2**, 781793 (2011).

[68] Z. Zhong, H. Song, T. Y. P. Chui, B. L. Petrig, and S. A. Burns, "Noninvasive measurements and analysis of blood velocity profiles in human retinal vessels," Investigative Ophthalmology & Visual Science **52**, 4151–4157 (2011).

[69] T. Y. P. Chui, D. A. VanNasdale, and S. A. Burns, "The use of forward scatter to improve retinal vascular imaging with an adaptive optics scanning laser ophthalmoscope," Biomedical Optics Express **3**, 2537 (2012).

[70] E. J. Fernández, B. Hermann, B. Považay, A. Unterhuber, H. Sattmann, B. Hofer, P. K. Ahnelt, and W. Drexler, "Ultrahigh resolution optical coherence tomography and pancorrection for cellular imaging of the living human retina," Optics Express **16**, 11083–11094 (2008).

[71] C. Torti, B. Považay, B. Hofer, A. Unterhuber, J. Carroll, P. K. Ahnelt, and W. Drexler, "Adaptive optics optical coherence tomography at 120,000 depth scans/s for non-invasive cellular phenotyping of the living human retina," Opt. Express **17**, 19382–19400 (2009).

[72] O. P. Kocaoglu, S. Lee, R. S. Jonnal, Q. Wang, A. E. Herde, J. C. Derby, W. Gao, and D. T. Miller, "Imaging cone photoreceptors in three dimensions and in time using ultrahigh resolution optical coherence tomography with adaptive optics," Biomedical Optics Express **2**, 748–763 (2011).

[73] D. X. Hammer, N. V. Iftimia, R. D. Ferguson, C. E. Bigelow, T. E. Ustun, A. M. Barnaby, and A. B. Fulton, "Foveal fine structure in retinopathy of prematurity: An adaptive optics fourier domain optical coherence tomography study," Investigative Ophthalmology & Visual Science **49**, 2061 –2070 (2008).

[74] R. J. Zawadzki, S. S. Choi, S. M. Jones, S. S. Oliver, and J. S. Werner, "Adaptive optics-optical coherence tomography: optimizing visualization of microscopic retinal structures in three dimensions," J. Opt. Soc. Am. A **24**, 1373–1383 (2007).

[75] Q. Wang, O. P. Kocaoglu, B. Cense, J. Bruestle, R. S. Jonnal, W. Gao, and D. T. Miller, "Imaging retinal capillaries using ultrahigh-resolution optical coherence tomography and adaptive optics." Invest Ophthalmol Vis Sci **52**, 6292–6299 (2011).

[76] K. Kurokawa, K. Sasaki, S. Makita, Y.-J. Hong, and Y. Yasuno, "Three-dimensional retinal and choroidal capillary imaging by power doppler optical coherence angiography with adaptive optics," Optics Express **20**, 22796–22812 (2012).

[77] K. Kurokawa, D. Tamada, S. Makita, and Y. Yasuno, "Adaptive optics retinal scanner for one-micrometer light source," Opt. Express **18**, 1406–1418 (2010).

[78] K. Kurokawa, K. Sasaki, S. Makita, M. Yamanari, B. Cense, and Y. Yasuno, "Simultaneous high-resolution retinal imaging and high-penetration choroidal imaging by one-micrometer adaptive optics optical coherence tomography," Optics Express **18**, 8515–8527 (2010).

[79] K. Sasaki, K. Kurokawa, S. Makita, and Y. Yasuno, "Extended depth of focus adaptive optics spectral domain optical coherence tomography," Biomedical Optics Express **3**, 2353–2370 (2012).

[80] B. Potsaid, B. Baumann, D. Huang, S. Barry, A. E. Cable, J. S. Schuman, J. S. Duker, and J. G. Fujimoto, "Ultrahigh speed 1050nm swept source / fourier domain OCT retinal and anterior segment imaging at 100,000 to 400,000 axial scans per second," Opt. Express **18**, 20029E0048 (2010).

[81] T. Klein, W. Wieser, C. M. Eigenwillig, B. R. Biedermann, and R. Huber, "Megahertz OCT for ultrawide-field retinal imaging with a 1050nm fourier domain mode-locked laser," Optics Express **19**, 3044–3062 (2011).

[82] B. Potsaid, V. Jayaraman, J. G. Fujimoto, J. Jiang, P. J. S. Heim, and A. E. Cable, "Mems tunable vcsel light source for ultrahigh speed 60khz - 1mhz axial scan rate and long range centimeter class oct imaging," Proceedings of SPIE **8213**, 82130M–82130M–8 (2012).

[83] M. Mujat, R. D. Ferguson, A. H. Patel, N. Iftimia, N. Lue, and D. X. Hammer, "High resolution multimodal clinical ophthalmic imaging system," Opt. Express **18**, 1160711621 (2010).

[84] S. Makita, T. Fabritius, and Y. Yasuno, "Full-range, high-speed, high-resolution 1-μm spectral-domain optical coherence tomography using BM-scan for volumetric imaging of the human posterior eye," Optics Express **16**, 8406–8420 (2008).

[85] J. Dowski and W. T. Cathey, "Extended depth of field through wave-front coding," Applied Optics **34**, 1859–1866 (1995).

[86] P. Dufour, M. Piché, Y. De Koninck, and N. McCarthy, "Two-photon excitation fluorescence microscopy with a high depth of field using an axicon," Applied Optics **45**, 9246–9252 (2006).

[87] E. Botcherby, R. Jvskaitis, and T. Wilson, "Scanning two photon fluorescence microscopy with extended depth of field," Optics Communications **268**, 253–260 (2006).

[88] Z. Ding, H. Ren, Y. Zhao, J. S. Nelson, and Z. Chen, "High-resolution optical coherence tomography over a large depth range with an axicon lens," Opt. Lett. **27**, 243245 (2002).

[89] R. A. Leitgeb, M. Villiger, A. H. Bachmann, L. Steinmann, and T. Lasser, "Extended focus depth for fourier domain optical coherence microscopy," Opt. Lett. **31**, 24502452 (2006).

[90] A. Burvall, K. Kołacz, Z. Jaroszewicz, and A. T. Friberg, "Simple lens axicon," Applied optics **43**, 4838–4844 (2004). PMID: 15449470.

[91] L. Xu, J. Li, T. Cui, A. Hu, G. Fan, R. Zhang, H. Yang, B. Sun, and J. B. Jonas, "Refractive error in urban and rural adult chinese in beijing," Ophthalmology **112**, 1676–1683 (2005).

[92] A. Sawada, A. Tomidokoro, M. Araie, A. Iwase, and T. Yamamoto, "Refractive errors in an elderly japanese population: The tajimi study," Ophthalmology **115**, 363–370.e3 (2008).

[93] E. J. Fernández, A. Unterhuber, B. Považay, B. Hermann, P. Artal, and W. Drexler, "Chromatic aberration correction of the human eye for retinal imaging in the near infrared," Optics Express **14**, 6213–6225 (2006).

[94] R. J. Zawadzki, B. Cense, Y. Zhang, S. S. Choi, D. T. Miller, and J. S. Werner, "Ultrahigh-resolution optical coherence tomography with monochromatic and chromatic aberration correction," Optics Express **16**, 8126–8143 (2008).

[95] H. Hofer, P. Artal, B. Singer, J. L. Aragón, and D. R. Williams, "Dynamics of the eye's wave aberration," Journal of the Optical Society of America A **18**, 497–506 (2001).

[96] P. Bedggood, M. Daaboul, R. Ashman, G. Smith, and A. Metha, "Characteristics of the human isoplanatic patch and implications for adaptive optics retinal imaging," Journal of Biomedical Optics **13**, 024008–024008–7 (2008).

[97] P. Artal, S. Marcos, R. Navarro, and D. R. Williams, "Odd aberrations and double-pass measurements of retinal image quality," Journal of the Optical Society of America A **12**, 195–201 (1995).

[98] J. Schwieqerling, *Field Guide to Visual and Ophthalmic Optics* (SPIE Publications, 2005).

[99] Z136Committee, *American National Standard for Safe Use of Lasers: ANSI Z136.1-2000* (Laser Institute of America, 2003).

[100] C. A. Curcio, K. R. Sloan, O. Packer, A. E. Hendrickson, and R. E. Kalina, "Distribution of cones in human and monkey retina: individual variability and radial asymmetry," Science **236**, 579–582 (1987).

[101] S. S. Choi, N. Doble, J. Lin, J. Christou, and D. R. Williams, "Effect of wavelength on in vivo images of the human cone mosaic," J. Opt. Soc. Am. A **22**, 25982605 (2005).

[102] C. Leahy, C. Leroux, C. Dainty, and L. Diaz-Santana, "Temporal dynamics and statistical characteristics of the microfluctuationsof accommodation: Dependence on the mean accommodative effort," Opt. Express **18**, 26682681 (2010).

[103] J. Flammer, S. Orgül, V. P. Costa, N. Orzalesi, G. K. Krieglstein, L. M. Serra, J.-P. Renard, and E. Stefánsson, "The impact of ocular blood flow in glaucoma," Progress in Retinal and Eye Research **21**, 359–393 (2002).

[104] M. A. Zarbin, "Current concepts in the pathogenesis of age-related macular degeneration," Archives of Ophthalmology **122**, 598–614 (2004). PMID: 15078679.

[105] C. J. Pournaras, E. Rungger-Brändle, C. E. Riva, S. H. Hardarson, and E. Stefansson, "Regulation of retinal blood flow in health and disease," Progress in Retinal and Eye Research **27**, 284–330 (2008).

[106] R. F. Gariano and T. W. Gardner, "Retinal angiogenesis in development and disease," Nature **438**, 960–966 (2005).

[107] M. Miura, S. Makita, T. Iwasaki, and Y. Yasuno, "Three-dimensional visualization of ocular vascular pathology by optical coherence angiography in vivo," Investigative Ophthalmology & Visual Science (2011).

[108] R. Flower, E. Peiretti, M. Magnani, L. Rossi, S. Serafini, Z. Gryczynski, and I. Gryczynski, "Observation of erythrocyte dynamics in the retinal capillaries and choriocapillaris using ICG-Loaded erythrocyte ghost cells," Investigative Ophthalmology $0 Visual Science **49**, 5510–5516 (2008).

[109] S. Makita, Y. Hong, M. Yamanari, T. Yatagai, and Y. Yasuno, "Optical coherence angiography," Opt. Express **14**, 7821–7840 (2006).

[110] L. An and R. K. Wang, "In vivo volumetric imaging of vascular perfusion within human retina and choroids with optical micro-angiography," Optics Express **16**, 11438–11452 (2008).

[111] A. Szkulmowska, M. Szkulmowski, D. Szlag, A. Kowalczyk, and M. Wojtkowski, "Three-dimensional quantitative imaging?of retinal and choroidal blood flow velocity using joint spectral and time domain optical coherence tomography," Optics Express **17**, 10584–10598 (2009).

[112] S. H. Yun, G. Tearney, J. de Boer, and B. Bouma, "Motion artifacts in optical coherence tomography with frequency-domain ranging," Optics Express **12**, 2977–2998 (2004).

[113] B. Park, M. C. Pierce, B. Cense, S.-H. Yun, M. Mujat, G. Tearney, B. Bouma, and J. de Boer, "Real-time fiber-based multi-functional spectral-domain optical coherence tomography at 1.3 m," Optics Express **13**, 3931–3944 (2005).

[114] J. Lee, V. Srinivasan, H. Radhakrishnan, and D. A. Boas, "Motion correction for phase-resolved dynamic optical coherence tomography imaging of rodent cerebral cortex," Optics Express **19**, 21258–21270 (2011).

[115] J. W. Goodman, *Speckle Phenomena in Optics Theory and Applications* (Roberts and Company, 2007).

[116] S. Singh Hayreh, "The choriocapillaris," Graefe's Archive for Clinical and Experimental Ophthalmology **192**, 165–179 (1974). 10.1007/BF00416864.

[117] R. W. Flower, A. W. Fryczkowski, and D. S. McLeod, "Variability in choriocapillaris blood flow distribution," Investigative Ophthalmology & Visual Science **36**, 1247–1258 (1995). PMID: 7775102.

[118] M. J. Hogan, J. A. Alvarado, and J. E. Weddell, *Histology of the Human Eye* (W.B. Saunders Company, 1971).